Differentiation of mammary tumors and reduction in metastasis upon *Malat1* lncRNA loss

Gayatri Arun,[1] Sarah Diermeier,[1] Martin Akerman,[1] Kung-Chi Chang,[1,2] J. Erby Wilkinson,[3] Stephen Hearn,[1] Youngsoo Kim,[4] A. Robert MacLeod,[4] Adrian R. Krainer,[1,2] Larry Norton,[5] Edi Brogi,[5] Mikala Egeblad,[1] and David L. Spector[1,2]

[1]Cold Spring Harbor Laboratory, Cold Spring Harbor, New York 11724, USA; [2]Molecular and Cellular Biology Program, Stony Brook University, Stony Brook, New York 11790, USA; [3]Department of Pathology, University of Michigan, Ann Arbor, Michigan 48109, USA; [4]Ionis Pharmaceuticals, Inc., Carlsbad, California 92010, USA; [5]Memorial Sloan Kettering Cancer Center, New York, New York 10065, USA

Genome-wide analyses have identified thousands of long noncoding RNAs (lncRNAs). *Malat1* (*metastasis-associated lung adenocarcinoma transcript 1*) is among the most abundant lncRNAs whose expression is altered in numerous cancers. Here we report that genetic loss or systemic knockdown of *Malat1* using antisense oligonucleotides (ASOs) in the *MMTV* (*mouse mammary tumor virus*)-*PyMT* mouse mammary carcinoma model results in slower tumor growth accompanied by significant differentiation into cystic tumors and a reduction in metastasis. Furthermore, *Malat1* loss results in a reduction of branching morphogenesis in *MMTV-PyMT*- and *Her2/neu*-amplified tumor organoids, increased cell adhesion, and loss of migration. At the molecular level, *Malat1* knockdown results in alterations in gene expression and changes in splicing patterns of genes involved in differentiation and protumorigenic signaling pathways. Together, these data demonstrate for the first time a functional role of *Malat1* in regulating critical processes in mammary cancer pathogenesis. Thus, *Malat1* represents an exciting therapeutic target, and *Malat1* ASOs represent a potential therapy for inhibiting breast cancer progression.

The majority of the mammalian genome encodes for noncoding RNAs (ncRNAs) (Derrien et al. 2012; Djebali et al. 2012; The ENCODE Project Consortium 2012). Long ncRNAs (lncRNAs) represent a class of ncRNAs that are >200 nucleotides (nt) and have been shown to participate in diverse cellular functions (for review, see Wilusz et al. 2009; Rinn and Chang 2012; Bergmann and Spector 2014). Over 16,000 lncRNAs have been annotated in the human genome, and, thus far, 8000 have been annotated in the mouse genome (Harrow et al. 2012). Several lncRNAs have been implicated in various types of cancer (for review, see Costa 2007; Prasanth and Spector 2007; Prensner and Chinnaiyan 2011). For example, *HOTAIR* is overexpressed in metastatic breast tumors and induces genome-wide repositioning of gene silencing complexes (Gupta et al. 2010). Multiple other lncRNAs such as *DD3/PCA3*, *PCAT-1*, and *SChLAP1* are overexpressed in prostate tumors (Bussemakers et al. 1999; Prensner et al. 2011, 2013), while the lncRNA *PVT1* was shown to regulate Myc protein levels in tumors with a 8q24 gain (Tseng et al. 2014).

MALAT1 (*metastasis-associated lung adenocarcinoma transcript 1*) is a highly conserved lncRNA that was first identified as being up-regulated in lung tumors that had a higher propensity to metastasize (Ji et al. 2003), and was subsequently shown to be up-regulated in a broad spectrum of tumor types (Yamada et al. 2006; Lin et al. 2007; Guffanti et al. 2009). *MALAT1* is among the most highly abundant lncRNAs, and, interestingly, its primary transcript is processed (Wilusz et al. 2008) into a long 6.7-kb transcript, which localizes to nuclear speckles (Hutchinson et al. 2007; Clemson et al. 2009; Bernard et al. 2010),

and a 61-nt tRNA-like small RNA, which localizes to the cytoplasm (Wilusz et al. 2008). *MALAT1* has been implicated in regulating alternative pre-mRNA splicing, and its knockdown was shown to result in cell cycle arrest (Tripathi et al. 2010). *MALAT1* has also been shown to be required to activate E2F target genes by repositioning them from polycomb bodies to transcriptionally active nuclear sites in a serum-dependent manner (Yang et al. 2011). More recently, two genome-wide studies have indicated that *MALAT1* binds to the transcription start sites (TSSs) and gene bodies of actively transcribing genes together with another lncRNA, *NEAT1* (West et al. 2014). In addition, a genome-wide RNA–RNA binding study has shown that *Malat1* can also bind to nascent pre-mRNAs indirectly via protein partners (Engreitz et al. 2014). Despite these functional insights derived from various cell lines, *Malat1* knockout mice developed in our laboratory and others (Eissmann et al. 2012; Nakagawa et al. 2012; Zhang et al. 2012) exhibit a normal phenotype. The mice are born in expected Mendelian ratios, and no major alterations have been observed in tissue histology, gene expression, or pre-mRNA splicing.

Although *Malat1* knockout mice have no overt phenotype, *MALAT1* loss in a lung cancer xenograft model resulted in reduced homing of human lung cancer cells to the lungs compared with control cells with wild-type levels of *MALAT1* (Gutschner et al. 2013), and knockdown of *MALAT1* in lung cancer cells in vitro impaired cellular motility (Tano et al. 2010; Gutschner et al. 2013). In addition, *MALAT1* gene mutations have been found to frequently occur in luminal-type breast tumors (Ellis et al. 2012). Based on these findings, we were interested in pursuing whether *Malat1* has a direct causative in vivo function in breast cancer progression.

Here we examined the role of *Malat1* in mammary tumor progression using the *MMTV* (*mouse mammary tumor virus*)-*PyMT* mouse mammary tumor model of human luminal B breast cancer (Guy et al. 1992; Lin et al. 2003; Herschkowitz et al. 2007). We found that genetic knockout of *Malat1* or knockdown upon subcutaneous delivery of antisense oligonucleotides (ASOs) resulted in significant differentiation of the primary tumors and a reduction in lung metastases. In addition, knockdown of *Malat1* in *MMTV-PyMT* and *Her2/neu*-amplified mammary tumor organoids inhibited branching morphogenesis ex vivo. Detailed molecular analyses by RNA sequencing (RNA-seq) revealed significant changes in gene expression and pre-mRNA splicing of protumorigenic and differentiation-related genes. These findings identify *Malat1* as a therapeutic target in breast cancer and the utility of *Malat1* ASOs as a therapeutic for inhibiting breast cancer progression.

Results

Mammary tumor progression is impaired upon genetic loss of *Malat1* lncRNA

Human luminal B breast cancer is one of the most prevalent subtypes of breast cancer, affecting nearly 15%–20% of individuals diagnosed with this disease (for review, see Schnitt 2010; Ades et al. 2014). In order to investigate the potential in vivo role of *Malat1* in mammary tumor progression, we used the *MMTV-PyMT* mouse mammary tumor model of human luminal B breast cancer (Guy et al. 1992; Lin et al. 2003; Herschkowitz et al. 2007). In this model, the polyoma middle-T antigen is under the control of the MMTV promoter, resulting in highly penetrant mammary tumors and lung metastasis (Lin et al. 2003).

Malat1 homozygous knockout (*Malat1$^{-/-}$*) female mice previously generated in our laboratory (Zhang et al. 2012) were crossed to *MMTV-PyMT* males (C57Bl/6) to obtain *MMTV-PyMT;Malat1$^{+/+}$*, *PyMT;Malat1$^{+/-}$*, and *PyMT; Malat1$^{-/-}$* mice. Individuals of all three genotypes were born in expected Mendelian ratios with a normal gestation period and postnatal development. In accord with published data (Lin et al. 2003), tumor onset in *MMTV-PyMT* mice began soon after puberty, and palpable tumors developed within 12–16 wk of birth in >90% of the mice. Tumor onset did not differ significantly in the presence or absence of *Malat1* (Fig. 1A). Prior to 5 mo of age, nearly 90% of the mice developed palpable multifocal mammary gland lesions, demonstrating that loss of *Malat1* does not affect the initiation of *PyMT*-induced mammary gland tumors. Although the tumors that developed in the *Malat1$^{-/-}$* background initially exhibited a relatively slower tumor growth rate compared with control mice (Fig. 1B), this difference was not found to be significant, especially at the later time points. Surprisingly, the *MMTV-PyMT;Malat1$^{-/-}$* mice developed highly cystic liquid-filled tumors (Fig. 1C, right panel), in contrast to the control mice, which developed poorly differentiated solid carcinomas (Fig. 1C, left panel). Hematoxylin and eosin (H&E) staining of tumor sections from *MMTV-PyMT; Malat1$^{-/-}$* mice demonstrated that nearly 90% of the tumors that were >1 cm in diameter exhibited a cystic phenotype, with >75% of the tumor area showing encapsulated well-differentiated cystic histopathology (Fig. 1D, bottom panels), in stark contrast to the poorly differentiated solid carcinomas observed in the control tumors (Fig. 1D, top panels).

In the *MMTV-PyMT* model, nearly 80% of the mice develop lung micro- and macrometastases. Therefore, we examined the impact of *Malat1* loss on lung metastases. *MMTV-PyMT;Malat1$^{-/-}$* mice exhibited a significant reduction in lung macrometastases, where only three of 12 mice had macro lesions as compared with seven of eight mice in control *MMTV-PyMT;Malat1$^{+/+}$* mice (Fig. 1E,F). The lungs were further examined for the incidence of micrometastases (Fig. 1G), and the majority of *MMTV-PyMT;Malat1$^{-/-}$* animals did not show any micrometastasis (nine of 12). Next, we calculated the total metastatic burden as a percentage of lung volume (Fig. 1H) and found that the *MMTV-PyMT;Malat1$^{-/-}$* animals showed a significantly decreased metastatic burden (3%–5%) as compared with the control *MMTV-PyMT;Malat1$^{+/+}$* mice, for which the metastatic burden reached up to 40% of the total lung volume. These results clearly demonstrate a role for the lncRNA *Malat1* in mammary tumor progression.
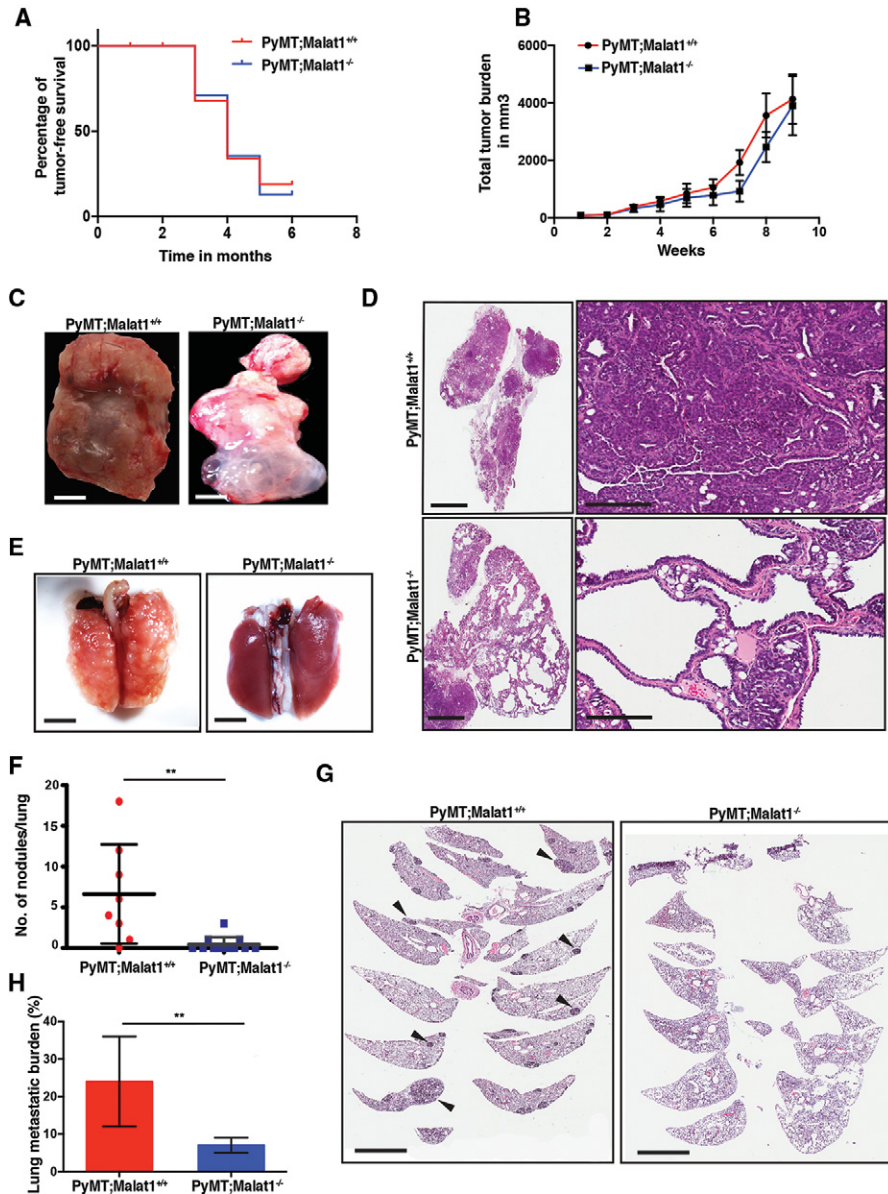
Figure 1. Impaired tumor progression and metastasis in *MMTV-PyMT* mice lacking *Malat1*. (*A*) Kaplan-Meier curves for tumor-free survival in *MMTV-PyMT;Malat1*$^{+/+}$ (*n* = 18) and *MMTV-PyMT;Malat1*$^{-/-}$ (*n* = 24) mice. (*B*) Total tumor burden in *MMTV-PyMT; Malat1*$^{+/+}$ (*n* = 8) and *MMTV-PyMT;Malat1*$^{-/-}$ (*n* = 12) mice from the detection of tumors (∼6 mm) over a period of 9 wk. Error bars represent SEM. (*C*) Surgically removed tumors from *MMTV-PyMT;Malat1*$^{+/+}$ (*left* panel) and *MMTV-PyMT;Malat1*$^{-/-}$ (*right* panel) mice. Bar, 2 mm. (*D*) H&E-stained sections of primary tumors from *MMTV-PyMT;Malat1*$^{+/+}$ and *MMTV-PyMT;Malat1*$^{-/-}$ mice. The entire tumor section and a higher magnification of a small region are shown from both genotypes. Bars: 2 mm and 200 μm for the different magnifications, respectively. (*E*) Whole-lung images showing lung metastatic nodules in *MMTV-PyMT;Malat1*$^{+/+}$ (*left* panel) compared with *MMTV-PyMT;Malat1*$^{-/-}$ (*right* panel). Bar, 5 mm. (*F*) Quantitation of number of macrometastatic nodules per lungs (total nodules/2). Error bars represent standard deviation (SD). (***) *P* < 0.001 by Wilcoxon signed rank test. (*G*) H&E-stained lung sections showing regions of micrometastasis in *MMTV-PyMT;Malat1*$^{+/+}$ lungs (*left* panel) and *MMTV-PyMT;Malat1*$^{-/-}$ lungs (*right* panel). Bar, 2 mm. (*H*) Percentage of lung metastatic burden over total lung area of *MMTV-PyMT;Malat1*$^{+/+}$mice (*n* = 7) and *MMTV-PyMT;Malat1*$^{-/-}$ mice (*n* = 4). Error bars represent SD. (***) *P* < 0.001 by Wilcoxon signed rank test.

MALAT1 *is up-regulated in human breast cancer metastases*

To understand the significance of *MALAT1* in human breast cancer, we evaluated its expression in human breast tumors by RNA-FISH on matched primary tumor and metastases tissue sections from the same individuals. *MALAT1* was generally expressed at a low level in the primary lesions (Fig. 2A, top panels) of breast tumors irrespective of the ER/PR status. However, very high levels of
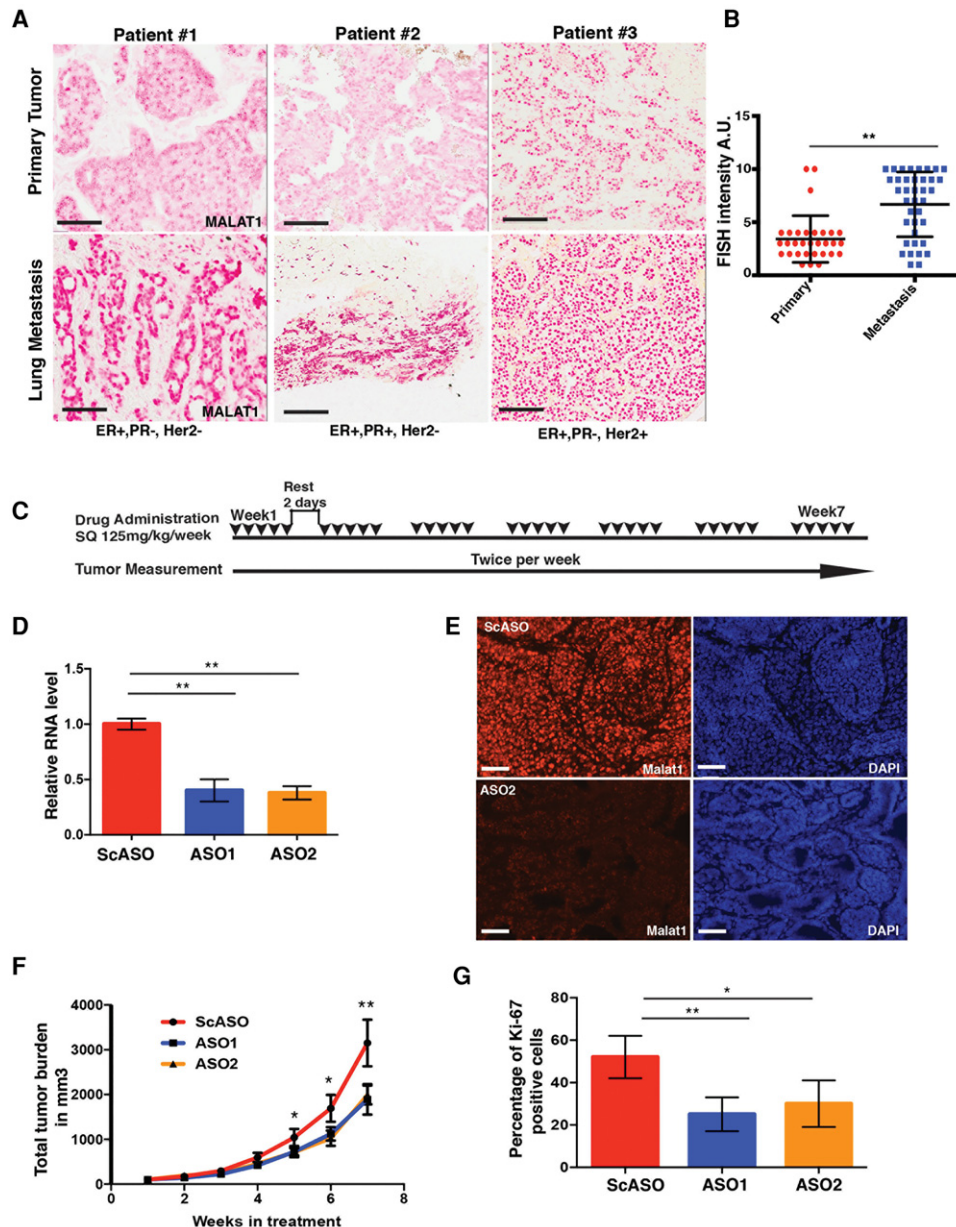
Figure 2. Efficient knockdown of *Malat1* in tumors using ASOs. (*A*) RNA-FISH using a *MALAT1*-specific probe on matched human primary tumor and lung metastases from breast cancer patients. Bar, 200 μm. Magnification scale is 15× using Aperio Scanscope. (*B*) Quantitation of *MALAT1* FISH signal in primary tumor and lung metastasis tissue array samples from breast cancer patients. (*C*) Schematic of the ASO treatment protocol in *MMTV-PyMT* mice. (*D*) RT-qPCR of *Malat1* knockdown in tumors of mice treated with scrambled ASO compared with *Malat1* ASO1 or ASO2. Relative fold change calculated based on the geometric mean of *Gapdh*, β-*actin*, and *Hprt* RNA levels. Error bars represent SD. (**) $P < 0.01$ by Student's t-test. (*E*) RNA-FISH of tumor sections using a *Malat1*-specific probe. Bar, 100 μm. Magnification scale is 20× using Aperio Scanscope. (*F*) Normalized tumor growth curve of *MMTV-PyMT* mice treated with control scrambled ASO (ScASO) ($n = 12$), *Malat1* ASO1 ($n = 11$), or *Malat1* ASO2 ($n = 7$). Error bars represent SEM. (*) $P < 0.05$; (**) $P < 0.01$ by ANOVA. (*G*) Percentage of Ki-67-positive cells in ScASO-treated tumors or *Malat1* ASO1- or ASO2-treated tumors. $n = 3$ tumors from each group, with at least two sections from each tumor. Error bars represent SD. (*) $P < 0.05$; (**) $P < 0.01$ by Student's t-test.

MALAT1 were observed in the lung metastases from the same individuals (Fig. 2A, bottom panels). Interestingly, higher levels of *MALAT1* expression were confined only to the tumor cells, while the adjacent stromal cells showed a very weak signal for *MALAT1* in both the primary tumor and the metastatic lesions (Supplemental Fig.

S1A). Some primary tumors showed elevated *MALAT1* expression in only a small fraction of the cancer cells or cell clusters, while neighboring cancer cells remained very low in *MALAT1* expression, suggesting that these high *MALAT1*-expressing cancer cells may escape the primary tumors preferentially to establish metastasis or that

potentially microenvironmental cues may influence *MALAT1* expression levels (Supplemental Fig. S1B,C). To determine the extent of occurrence of high *MALAT1* expression in human samples, we obtained a breast cancer tissue array and lung metastasis tissue array and evaluated *MALAT1* expression level using RNA-FISH. *MALAT1* transcript levels were increased between 1.5-fold and threefold in >60% of the lung metastases compared with the primary tumor sections (Fig. 2B). The lung metastasis array was generated from primary breast cancer patients. While only some of the primary tumor samples and lung metastases were matched, we could detect high *MALAT1* expression in the majority of the lung metastasis samples, confirming our matched sample data. High *MALAT1* expression was also observed in sections of human breast cancer brain metastatic lesions (Supplemental Fig. S1D). Interestingly, the MMTV-PyMT tumors also displayed a similar expression pattern for *Malat1*, where higher *Malat1* expression was confined to a small fraction of cells (Supplemental Fig. S2A–E). Furthermore, more higher *Malat1*-expressing cells were found in advanced carcinomas compared with adenomas or hyperplasia (Supplemental Fig. S2A–E). This observation suggests that *MALAT1* likely plays a crucial role in human breast cancer pathogenesis, prompting us to further evaluate its potential as a therapeutic target.

Knockdown of Malat1 *results in mammary tumor differentiation*

Next, we were interested in determining whether we could recapitulate the phenotype observed by genetic knockout upon systemically knocking down *Malat1* levels in established tumors in a more therapeutic setting. Since *Malat1* is a nuclear retained lncRNA, we used ASOs to achieve knockdown. *Malat1*-specific ASOs (16mers) were synthesized using a next-generation design comprised of phosphorothioate-modified short S-cEt (S-2′-O-Et-2′,4′-bridged nucleic acid) gapmer chemistry (Teplova et al. 1999). We used two independent *Malat1*-specific ASOs targeting two different regions of the *Malat1* transcript as well as a control scrambled ASO (ScASO).

Three-month-old to 4-mo-old mice were divided into three cohorts (seven to 12 mice each) and randomized based on their age, tumor size, and number of tumors. Each mouse in the cohort received either ScASO or *Malat1*-specific ASO1 or ASO2 via subcutaneous injections of 25 mg/kg per day (125 mg/kg per week) for 5 d with a rest period of 2 d (Fig. 2C). The injections were carried out for a period of 8 wk, upon which at least one tumor from most of the control mice reached 2 cm in size. During the course of the treatment, tumors were measured twice per week. At the end of the treatment period, the animals were euthanized, and the primary tumors and lungs were collected. An average *Malat1* knockdown of ∼60% was achieved in the mammary tumor tissue in mice treated with either ASO1 or ASO2 as compared with ScASO-treated control mice (Fig. 2D). Knockdown efficiency was also confirmed by RNA-FISH on tumor sec-

tions (Fig. 2E). Different regions of the treated tumors showed varying knockdown efficiencies ranging from 20% to 80% knockdown (data not shown).

Interestingly, when tumor growth was monitored over the course of treatment, the *Malat1* ASO-treated group showed a 50% slower tumor growth rate than tumors treated with ScASO (Fig. 2F). The decrease in growth rate was observed as early as week 3 into the treatment period, and, by the end of the treatment, the tumor volume was reduced by 50% in *Malat1* ASO-treated mice compared with the ScASO-treated group. Consistent with the slower tumor growth rate, Ki-67 labeling of the tumor sections showed a marked decrease in Ki-67-positive nuclei. The proliferative index of *Malat1* ASO1- or ASO2-treated tumors, calculated as a measure of Ki-67 positivity, was found to be 22% and 26%, respectively, compared with 51% in the control tumors treated with ScASO (Fig. 2G). Although this was in contrast to the knockout experiment, where there was no significant difference in primary tumor growth rate, we reason that this was due to the fact that the *Malat1* knockout tumors were extensively cystic, and, when we measured the tumor volume, it is likely that the cyst growth contributed significantly to the total volume rather than actual tumor mass.

The primary tumors from each group were analyzed for histopathological changes. Notably, the *Malat1* ASO-treated tumors were cystic, liquid-filled, encapsulated, well-differentiated primary tumors closely resembling those from the *MMTV-PyMT;Malat1$^{-/-}$* animals, whereas the tumors in the ScASO-treated control animals remained poorly differentiated, as in tumors from *MMTV-PyMT;Malat1$^{+/+}$* mice (Fig. 3A). Also, similar to the knockout phenotype, a single layer of epithelial cells lined the enlarged ducts in the *Malat1* ASO-treated mice. There was a significant increase in cystic/ductular tumors (31% in ASO1-treated and 22% in ASO2-treated) (Fig. 3B), whereas only 4% of the ScASO-treated mice developed cystic tumors similar in morphology to the *Malat1* ASO-treated groups. Furthermore, there was a twofold decrease in the number of solid carcinomas, characterized by poorly differentiated cells, in *Malat1* ASO-treated mice. Quantitation of the cystic area of *Malat1* ASO-treated tumors showed that, on average, 40% of the total tumor area contained cystic/ductular histopathology (Fig. 3C).

Given that *Malat1* ASO-treated tumors display a remarkable histological differentiation phenotype, we assayed for differentiation markers by immunofluorescence on sections of primary tumors. E-cadherin, a major cell adhesion protein present on the cell membrane of differentiated epithelial cells, exhibited increased labeling on the cell membrane of *Malat1* ASO-treated tumors (Fig. 3D, bottom panels), whereas the control tumors showed lower levels to undetectable levels of E-cadherin in several regions within the tumors of the control mice (Fig. 3D, top panels). Surprisingly, intense β-casein localization was observed in the enlarged ducts of *Malat1* ASO-treated tumors (Fig. 3E, bottom panels), consistent with the differentiation phenotype. In contrast, β-casein was absent in the control tumor sections (Fig. 3E, top panels).
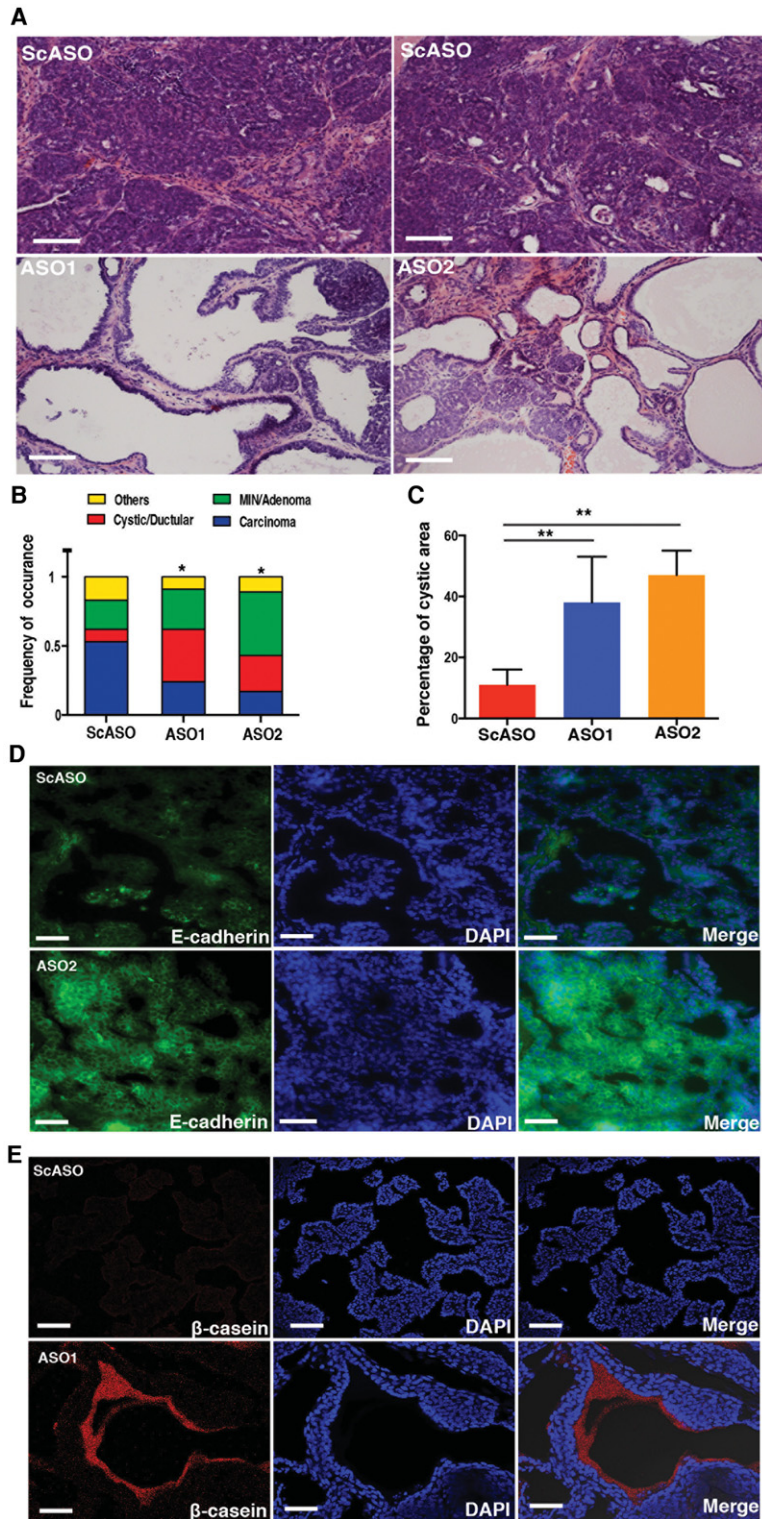
Figure 3. *Malat1* knockdown results in differentiation of MMTV-PyMT tumors. (*A*) Representative H&E-stained primary tumor sections from mice treated with ScASO (*top* panels) or *Malat1* ASO1 or ASO2 (*bottom* panels). Bar, 100 μm. (*B*) The frequency of occurrence of different histologic grades in scrambled versus *Malat1* ASO-treated tumor sections stained with H&E. $n \geq 20$ tumors from each group. (*) $P < 0.05$ by Fisher's exact test. (*C*) Percentage of cystic area in the tumor sections from scrambled ($n = 4$) versus *Malat1* ASO1-treated ($n = 6$) and ASO2-treated ($n = 4$) mice. Error bars represent SD. (**) $P < 0.01$ by Wilcoxon signed rank test. (*D*) Representative E-cadherin immunolabeling on cryosections of tumors from ScASO- or *Malat1* ASO2-treated mice. Bars, 100 μm. (*E*) Representative β-casein immunolabeling on cryosections of tumors from ScASO-treated mice or *Malat1* ASO1-treated mice. Bars, 100 μm.

Malat1 *ASO treatment significantly reduces lung metastasis*

Given the reduction of metastasis seen in the *MMTV-PyMT;Malat1*$^{-/-}$ animals (Fig. 1E–H), it was important to determine whether *Malat1* knockdown could also result in a reduction in the incidence of lung metastasis in this therapeutic setting. Indeed, *Malat1* ASO treatment resulted in a significant reduction in lung metastatic incidence (Fig. 4A). A small fraction of *Malat1* ASO-treated
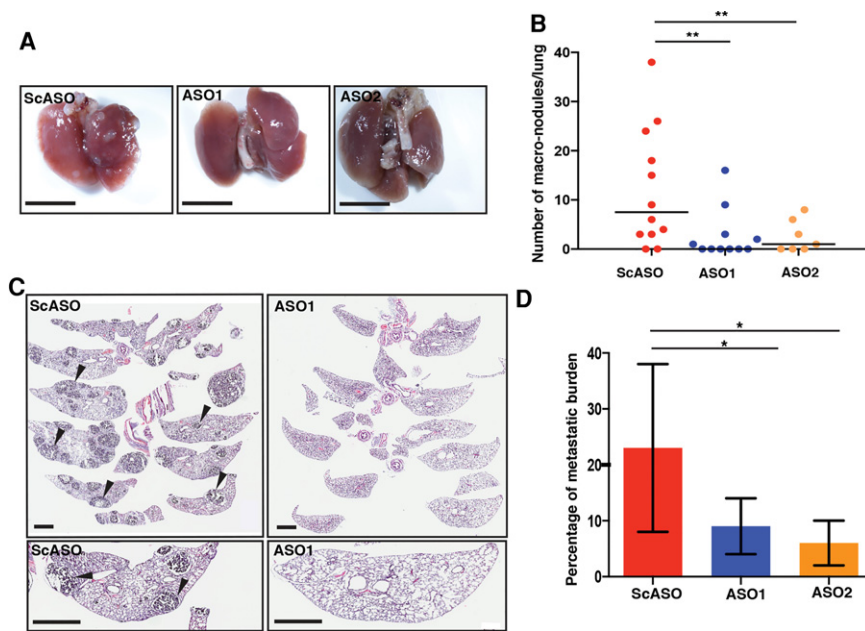
Figure 4. Lung metastasis is impaired in *Malat1* knockdown mice. (*A*) Representative lungs with metastatic nodules from ScASO-treated and *Malat1* ASO1- or ASO2-treated mice. (*B*) Quantitation of lung metastatic nodules from ScASO-treated and *Malat1* ASO1- or ASO2-treated mice. Each dot represents one mouse. (*) $P < 0.05$; (**) $P < 0.01$ by Wilcoxon signed rank test. (*C*) Representative H&E-stained lung sections from ScASO-treated and *Malat1* ASO1-treated mice. Arrowheads indicate representative micrometastases. Bar, 2 mm. (*D*) Quantitation of the percentage of lung metastatic burden from ScASO-treated and *Malat1* ASO1- or ASO2-treated mice. $n = 5$ lung sections from each group. Error bars represent SD. (*) $P < 0.05$ by Wilcoxon signed rank test.

animals (six of 18) developed macrometastatic nodules as compared with the control mice (10 of 12) (Fig. 4B). Furthermore, the lungs were serial-sectioned to determine the incidence of micrometastases and obtain the total metastatic burden for a given lung volume. Consistent with data obtained from genetic loss of *Malat1* (Fig. 1E–H), the *Malat1* ASO-treated group showed a significantly reduced metastatic burden (<10%) (Fig. 4C,D) compared with the larger metastatic burden (>30%) observed in the ScASO-treated group. Micrometastases were also not observed in lungs that were free of macrometastatic nodules in mice treated with *Malat1* ASOs. The livers and brains from the *Malat1* ASO-treated groups and control groups were also analyzed for metastatic incidence, and no evidence of macrometastatic lesions was found in those organs (data not shown). Thus, we conclude that *Malat1* loss impairs the metastatic progression of the disease. As such *Malat1* ASOs represent a potent therapeutic approach for metastatic breast cancer.

Malat1 *loss affects branching morphogenesis in tumor-derived organoids*

Three-dimensional (3D) organotypic culture systems allow studies of physiologically relevant cellular processes as well as disease states under defined culture conditions (Ewald et al. 2008; for review, see Sato and Clevers 2013; Sachs and Clevers 2014). Mammary gland organoids preserve the gland characteristics and undergo various morphogenetic changes upon growth factor stimulus that recapitulate normal physiological processes such as branching morphogenesis (Ewald et al. 2008; Cheung et al. 2013). To investigate the role of *Malat1* in these processes, organoids were prepared from *MMTV-PyMT* tumors <1 cm in size. These tumor organoids were grown on Matrigel for up to 6 d in the presence or absence of *Malat1* ASOs, allowing us to track growth, dynamics, and branching morphogenesis of the organoids (Fig. 5A).

The *Malat1* ASOs were taken up "freely" by the organoids without the use of transfection reagents, and an ~90% knockdown of the *Malat1* transcript was achieved with either *Malat1* ASO relative to the ScASO control (Fig. 5B). After 6 d in culture, mock-treated organoids or ScASO-treated organoids underwent extensive branching morphogenesis (Fig. 5C [top panels], D). In contrast, organoids treated with *Malat1* ASO1 or ASO2 failed to undergo branching morphogenesis (Fig. 5C [bottom panels], D) and remained as spherical acini that were smaller than the branched control organoids. The loss of branching was found to be specific for ASOs targeting *Malat1*, as knockdown of *Neat1*, another nuclear lncRNA encoded in the same chromosomal region as *Malat1*, resulted in organoids with branching morphogenesis similar to control *PyMT* tumor organoids (Supplemental Fig. S3A). Furthermore, detailed time-lapse differential interference contrast (DIC) imaging showed that control organoids underwent active remodeling throughout the imaging window (4 d), displaying extensive movement within the Matrigel (Supplemental Movie S1). The mock-treated or ScASO-treated organoids expanded rapidly, forming lumens, and, as early as 72 h, initiated the branching process (Supplemental Movie S1). Numerous cells migrated within the organoids, and these cells could be followed using organoids developed from *MMTV-PyMT;CAG::H2B-GFP* bitransgenic mice treated with ScASO (Supplemental Movie S3). In contrast, *Malat1* ASO1- or ASO2-treated organoids remained in the same position over the 84-h time course of imaging and did not show collective cell migration within the Matrigel (Supplemental Movie S2). Most importantly, cells within individual *Malat1* ASO-treated organoids also lacked cellular motility, and the
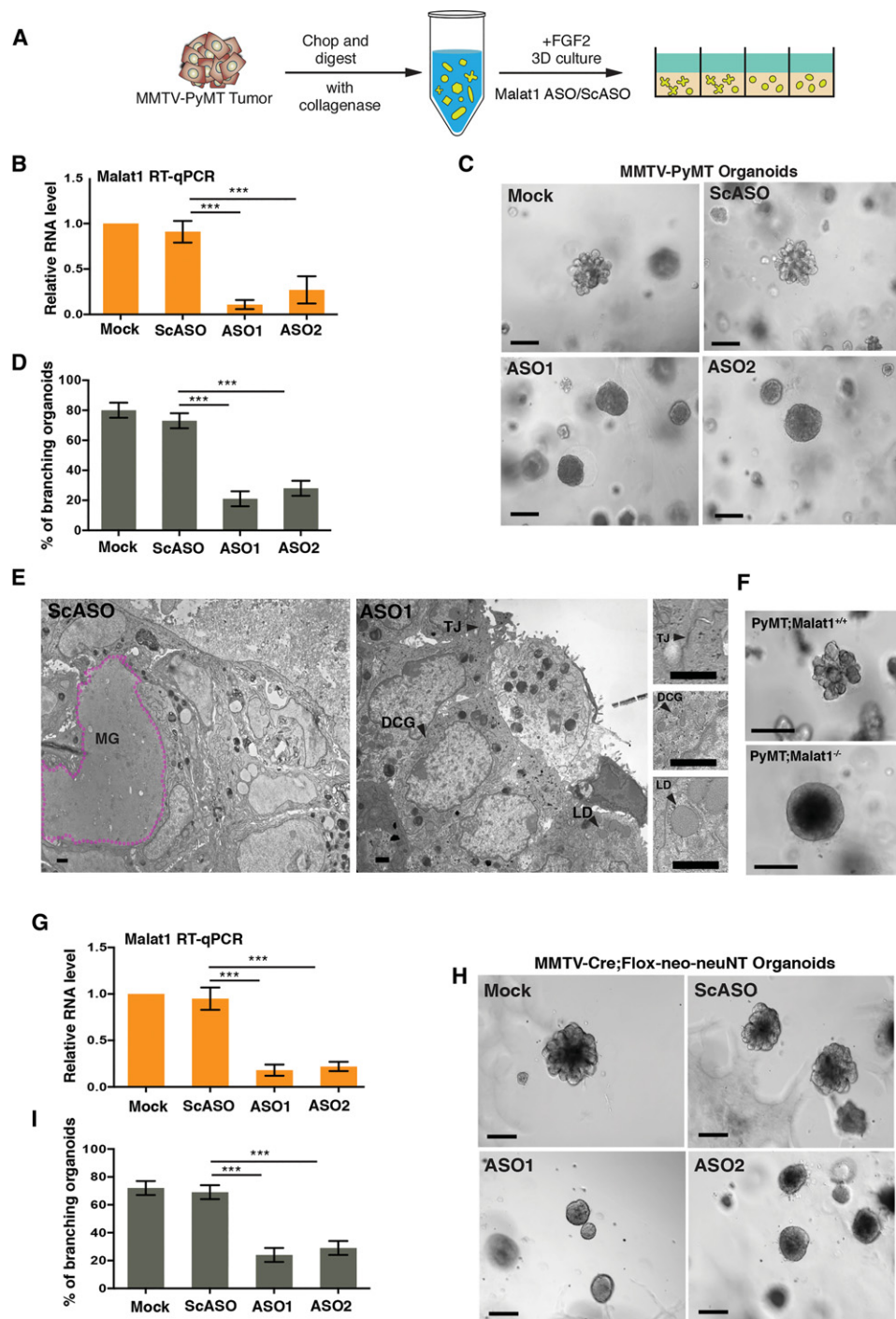
Figure 5. *Malat1* knockdown affects branching morphogenesis in the tumor-derived organoids. (*A*) Schematic of preparation of tumor-derived organoids. (*B*) qRT–PCR of relative *Malat1* RNA level in *MMTV-PyMT* tumor-derived organoids mock-treated or treated with ScASO or *Malat1* ASO1 or ASO2. *n* = 4 independent experiments. Error bars represent SD. (*C*) Differential interference contrast (DIC) images of organoids that were mock treated or treated with ScASO or *Malat1* ASO1 or ASO2 after 6 d of culturing. Mock represents PBS-treated organoids. Bar, 125 µm. (*D*) Percentage of branched organoids from PyMT tumors subjected to mock, ScASO, or *Malat1* ASO1 or ASO2 treatments. *n* = ≥ 200 organoids from four biological replicates. Error bars represent SD. (*E*) Representative transmission electron microscopy (TEM) images of a ScASO-treated PyMT organoid showing loosely opposed tumor cells with prominent internal deposit of Matrigel material (MG) and a *Malat1* ASO1-treated PyMT organoid showing closely opposed polarized tumor cells with tight junctions (TJs) and evidence of secretory dense-core granules (DCGs) and lipid droplets (LDs). The *insets* are higher-magnification images of tight junctions, dense-core granules, and lipid droplets. Bars, 1 µm. (*F*) DIC images of tumor organoids from *MMTV-PyMT;Malat1^{+/+}* (*top* panel) and *MMTV-PyMT;Malat1^{−/−}* (*bottom* panel). Bar, 100 µm. (*G*) RT-qPCR of relative *Malat1* RNA level in *MMTV-Cre;FL-neo-NeuNT* tumor-derived organoids. *n* = 3 biological replicates. Error bars represent SD. (*H*) DIC image of *MMTV-Cre;FL-neo-NeuNT* organoids treated with mock, ScASO, and *Malat1* ASO1 and ASO2 after 6 d of culturing. Bar, 125 µm. (*I*) Percentage of branched organoids from *MMTV-Cre; FL-neo-NeuNT* tumors subjected to treatment. *n* = ≥80 organoids from three biological replicates. Error bars represent SD.
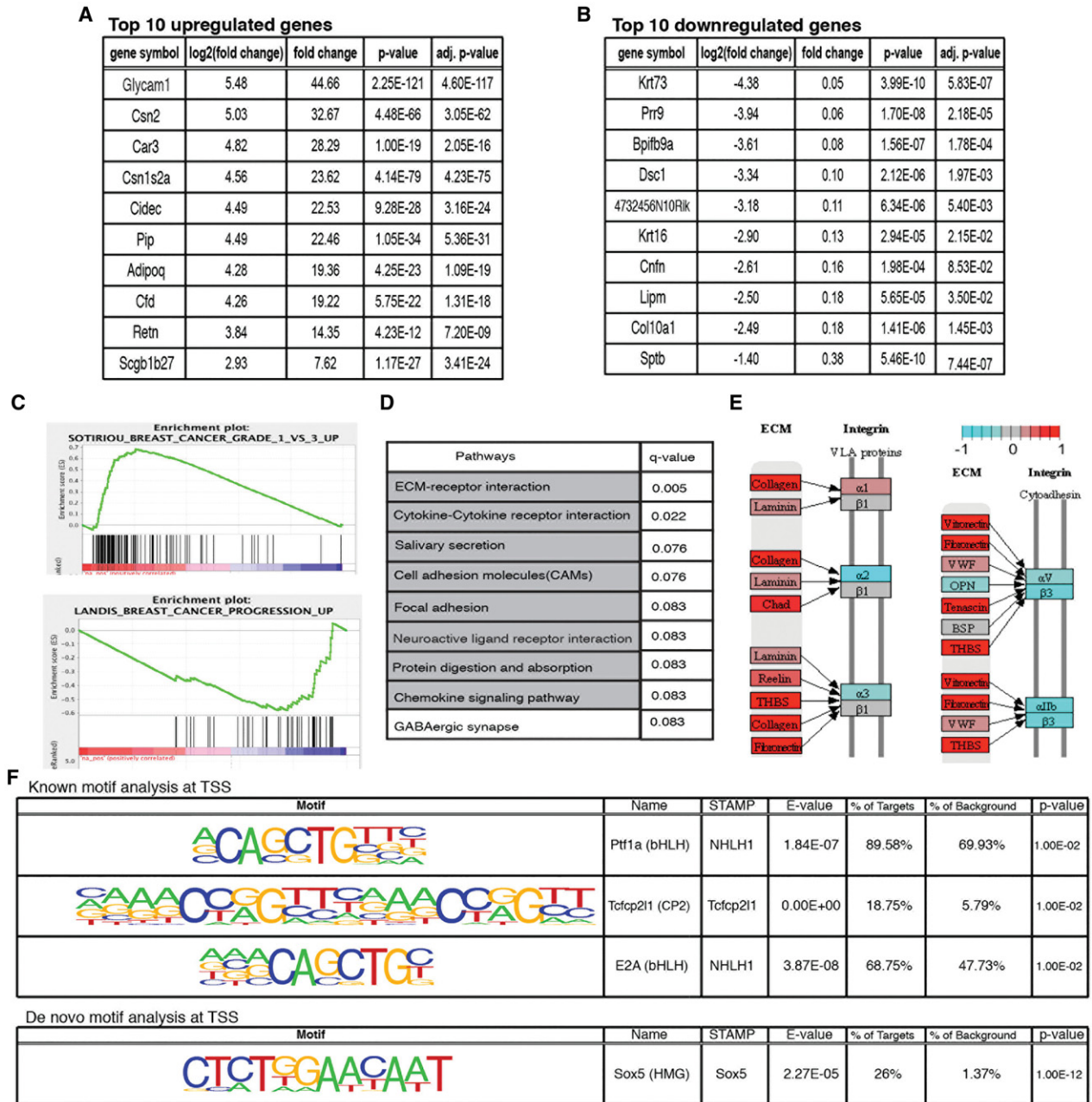
organoids appeared highly compact (Supplemental Movie S4). Interestingly, organoids treated with *Malat1* ASOs showed increased apoptotic cell death and a significant reduction in the number of dividing cells (Supplemental Fig. S3B).

To further characterize the distinct morphological change induced upon *Malat1* ASO treatment, transmission electron microscopic analysis was performed on the organoids to evaluate ultrastructural differences (Fig. 5E; Supplemental Fig. S3C). Consistent with the differentiation phenotype observed in the tumors treated with *Malat1* ASOs, the organoids also showed well-differentiated subcellular structures, such as the presence of secretory lipid droplets and dense core granules that were absent in the control organoids treated with ScASO or PBS. Importantly, *Malat1* ASO-treated organoids exhibited tight cell–cell contacts with little to no intercellular spaces. An increase in cell–cell junctional complexes such as desmosomes was observed in *Malat1* ASO-treated organoids compared with the control branched organoids (Supplemental Fig. S3C). Consistent with this observation, desmosomes have previously been shown to negatively regulate branching morphogenesis (Basham et al. 2013). The cells within the *Malat1* ASO-treated organoids were aligned adjacent to each other in a polarized manner with intercellular ducts that are present in normal mammary glands; these ducts are one of the distinct features of differentiated epithelial cells (Zhan et al. 2008; Watson and Campbell 2009). The ScASO- or mock-treated PyMT organoids lacked polarity, and the vast majority of the organoids contained Matrix proteins within the organoids, which reflected the active extracellular matrix (ECM) remodeling necessary for migration (Supplemental Fig. S3C). Last, organoids derived from *MMTV-PyMT*; *Malat1*$^{-/-}$ tumors did not undergo branching morphogenesis and remained as spherical tightly packed acini (Fig. 5F), whereas the *MMTV-PyMT;Malat1*$^{+/+}$ organoids were extensively branched. The loss of branching phenotype observed in the *MMTV-PyMT;Malat1*$^{-/-}$ organoids could be rescued by full-length mouse *Malat1* that was nucleofected into those organoids (Supplemental Fig. S4A–D). We observed ~30% branching in *MMTV-PyMT*; *Malat1*$^{-/-}$ organoids that were nucleofected with full-length mouse *Malat1.* In contrast, 5% of organoids displayed branching in mock transfected or GFP transfected organoids (Supplemental Fig. S4D). The nucleofection efficiency ranged between 35% and 45% (data not shown). The effect of *Malat1* knockdown was also studied in organoids derived from *MMTV-cre;Flox-neo-neuNT* mice, a model that phenocopies the *HER2*-amplified subtype of human breast cancer. Here, the first exon of endogenous *neu* (mouse homolog of *HER2/ERBB2*) has been replaced with *Cre*-inducible activated *neu*-cDNA, resulting in constitutively active Neu protein transcribed from its endogenous promoter in mammary epithelial cells (Andrechek et al. 2000). Control organoids derived from this model underwent branching morphogenesis, while the *Malat1* ASO-treated organoids failed to undergo branching morphogenesis, resulting in the formation of tightly packed spherical acinar structures (Fig. 5G–I).

Malat1 *knockdown in tumors disrupts protumorigenic signaling pathways*

Next, we sought to investigate the gene expression changes that are triggered upon *Malat1* knockdown in both tumor organoids and primary tumors by RNA-seq. RNA was isolated from day 6 organoids that were either untreated mock control or treated with ScASO or *Malat1* ASO1 or ASO2. We used tumors from four *MMTV-PyMT* mice to prepare organoids that were subjected to different ASO intervention. The differentially expressed genes in *Malat1* ASO1- or ASO2-treated organoids or tumor sections were compared with ScASO- or mock-treated controls. When we subjected the entire organoid data set to pathway analysis using the Kyoto Encyclopedia of Genes and Genomes (KEGG), several tumorigenic signaling pathways were enriched. Interestingly, enrichment of genes belonging to the ECM receptor, focal adhesion, and cell adhesion pathways was observed (false discovery rate [FDR] < 0.1) (Supplemental Table S1). These pathway changes are highly consistent with the phenotypic changes observed in the organoids upon *Malat1* ASO treatment; i.e., loss of cellular migration and increased adhesion observed by the loss of branching morphogenesis.

RNA-seq analysis was also carried out from tumors derived from *Malat1* ASO1- or ASO2-treated mice that were compared with tumors from ScASO-treated mice, and 52 genes were affected upon *Malat1* ASO treatment, with a significance threshold of FDR < 0.1 (Supplemental Fig. S5A). Additionally, 478 genes were found to be differentially expressed; these genes were filtered based on fold change cutoff from both ASO1- and ASO2-treated tumors and exhibited a significant change in one or the other treated tumors (Supplemental Table S2). The sample correlation plot also reflected the heterogeneity between the tumors. Nevertheless, the top 10 up-regulated and down-regulated genes from the tumors were indeed very interesting candidates (Fig. 6A,B). Of the up-regulated genes, the casein gene family was significantly enriched. This included *Csn2* that encodes for the β-casein protein, the major milk protein, and *Csn1s2a*, a member of the α-casein family. Additionally, *Wap* (whey acidic protein), *Lao*, and *Cel*, which are also constituents of mammalian milk, were also up-regulated in many of the tumors. In light of the significant differentiation phenotype that was observed in the *Malat1* ASO-treated tumors, it was reassuring to observe that these genes were also up-regulated >20-fold in these tumors. Additionally, up-regulation of the *Pip* gene is a confirmation of the cystic phenotype, as Pip (also known as gross mammary gland cystic fluid) is a protein that is secreted in cystic mammary gland lesions (Collette et al. 1986). Many of the lactation-related genes were validated by RT-qPCR from the ASO-treated tumors as well as *Malat1* knockout tumors (Supplemental Fig. S5B). Interestingly, none of the genes genomically adjacent to *Malat1* showed significant expression change except *Cdc42ep2*, which showed 1.3-fold up-regulation in the ASO-treated tumors. We subjected the entire data set to gene set enrichment analysis (GSEA) (Subramanian et al. 2005; Luo et al. 2009), and, interestingly, significant

A Top 10 upregulated genes

gene symbol	log2(fold change)	fold change	p-value	adj. p-value
Glycam1	5.48	44.66	2.25E-121	4.60E-117
Csn2	5.03	32.67	4.48E-66	3.05E-62
Car3	4.82	28.29	1.00E-19	2.05E-16
Csn1s2a	4.56	23.62	4.14E-79	4.23E-75
Cidec	4.49	22.53	9.28E-28	3.16E-24
Pip	4.49	22.46	1.05E-34	5.36E-31
Adipoq	4.28	19.36	4.25E-23	1.09E-19
Cfd	4.26	19.22	5.75E-22	1.31E-18
Retn	3.84	14.35	4.23E-12	7.20E-09
Scgb1b27	2.93	7.62	1.17E-27	3.41E-24

B Top 10 downregulated genes

gene symbol	log2(fold change)	fold change	p-value	adj. p-value
Krt73	-4.38	0.05	3.99E-10	5.83E-07
Prr9	-3.94	0.06	1.70E-08	2.18E-05
Bpifb9a	-3.61	0.08	1.56E-07	1.78E-04
Dsc1	-3.34	0.10	2.12E-06	1.97E-03
4732456N10Rik	-3.18	0.11	6.34E-06	5.40E-03
Krt16	-2.90	0.13	2.94E-05	2.15E-02
Cnfn	-2.61	0.16	1.98E-04	8.53E-02
Lipm	-2.50	0.18	5.65E-05	3.50E-02
Col10a1	-2.49	0.18	1.41E-06	1.45E-03
Sptb	-1.40	0.38	5.46E-10	7.44E-07

C

D

Pathways	q-value
ECM-receptor interaction	0.005
Cytokine-Cytokine receptor interaction	0.022
Salivary secretion	0.076
Cell adhesion molecules(CAMs)	0.076
Focal adhesion	0.083
Neuroactive ligand receptor interaction	0.083
Protein digestion and absorption	0.083
Chemokine signaling pathway	0.083
GABAergic synapse	0.083

E

F

Known motif analysis at TSS

Motif	Name	STAMP	E-value	% of Targets	% of Background	p-value
	Ptf1a (bHLH)	NHLH1	1.84E-07	89.58%	69.93%	1.00E-02
	Tcfcp2l1 (CP2)	Tcfcp2l1	0.00E+00	18.75%	5.79%	1.00E-02
	E2A (bHLH)	NHLH1	3.87E-08	68.75%	47.73%	1.00E-02

De novo motif analysis at TSS

Motif	Name	STAMP	E-value	% of Targets	% of Background	p-value
	Sox5 (HMG)	Sox5	2.27E-05	26%	1.37%	1.00E-12

Figure 6. Knockdown of *Malat1* affects tumor progression by altering many signaling pathways. (*A*) Top 10 significantly up-regulated genes. (*B*) Top 10 significantly down-regulated genes. (*C*) GSEA of tumor data sets showing enrichment of genes that affect tumor progression upon *Malat1* knockdown. (*D*) List of pathways that were significantly affected in tumors after *Malat1* ASO1 or ASO2 treatment compared with a ScASO-treated control. Highlighted in gray are common pathways that are affected in both organoids and tumors. (*E*) Representative example of the integrin pathway that was significantly altered in *Malat1* ASO-treated tumors versus the control. (*F*) De novo and known motif analyses of the promoters of differentially expressed genes.

enrichment of several gene sets involved in mammary tumor progression was observed (Fig. 6C), indicating that loss of *Malat1* inhibits several gene expression programs involved in tumor progression. Detailed pathway analysis using KEGG also resulted in enrichment of genes belonging to the ECM signaling, focal adhesion, and cell adhesion pathways (Fig. 6D). Nearly 90% of the tumor RNA-seq enriched pathways (eight of nine) were also enriched

in the organoid RNA-seq data analysis. One of the most significantly affected pathways was integrin signaling, with many of the protumorigenic integrins (*Itga2b* and *Itga5b3*) being down-regulated in *Malat1*-depleted tumors (Fig. 6E). To identify the transcription factors potentially cooperating with *Malat1*, we performed both known and de novo motif analysis of the promoter region (−900, +100 in relation to the TSS) of the differentially expressed

genes, and they showed significant enrichment in the Sox5-, Tcfcp2l1-, and E2A-binding motifs in their promoter regions (Fig. 6F). In addition, we took a sequence-independent approach by searching for overlaps between *Malat1* putative targets and >359 ChIP-seq (chromatin immunoprecipitation [ChIP] combined with deep sequencing) and ChIP–ChIP experiments annotated in the ChIP Enrichment Analysis (ChEA) database. From a total of 140 transcription factors, Sox9 was identified as a top scorer ($P = 0.0002$). Sox9 is a HMG protein that shares the similar DNA-binding element that was predicted for Sox5 in our motif analysis (data not shown). Interestingly, when comparing differentially expressed genes upon *Malat1* knockdown to CHART-seq (West et al. 2014) performed in MCF7 cells, we found that 11% of our differentially expressed genes possessed *MALAT1* peaks (Supplemental Table S3), suggesting that *Malat1* could directly regulate gene expression by physically binding to regulatory regions of those genes. Interestingly, one of the up-regulated genes, *Tnxb* (Tenascin Xb), an ECM protein that has been shown to have anti-metastatic properties (Matsumoto et al. 2001), had five *Malat1*-binding peaks with high peak scores (Supplemental Table S3).

Malat1 *knockdown affects multiple splicing events*

As *Malat1* has been implicated in alternative pre-mRNA splicing regulation in several cell lines (Tripathi et al. 2010) and in modulating the recruitment of splicing factors to an actively transcribing transgene reporter (Bernard et al. 2010), we investigated whether *Malat1* knockdown also resulted in changes in the in vivo splicing pattern of genes involved in tumorigenesis. The SpliceTrap/SpliceDuo pipeline (Wu et al. 2011) was applied to the RNA-seq data sets generated from the tumors and organoids. SpliceTrap performs probabilistic inference of the extent to which an exon is included in the mature transcript, is skipped, or is subjected to size variations due to alternative 3′/5′ splice sites or intron retention. SpliceDuo implements a noise-based methodology to identify statistically significant alternative splicing events across two conditions (see Supplemental Fig. S6A for splicing analysis pipeline). Interestingly, numerous alternative splicing changes were observed in both the *Malat1* ASO-treated tumors and organoids when compared with the ScASO-treated samples (Fig. 7A,B; Supplemental Table S4). We detected a total of 1351 splicing changes spanning the four major classes of alternative splicing patterns in at least two biological replicates, resulting in a 60% overlap between ASO1 and ASO2 treatment (Fig. 7B). This finding suggests an involvement of *Malat1* in alternative splicing of many important genes. Interestingly, *Esr1* coding for estrogen receptor α (ERα) was found to be alternatively spliced in its 5′ untranslated region (UTR) in *Malat1* ASO-treated samples compared with ScASO-treated tumors (Fig. 7C; Supplemental Table S4). When we looked at ERα protein expression using immunoblot analysis (Supplemental Fig. S6B), we observed that the control tumors showed lower ERα expression compared with *Malat1* ASO-treated tumors. It is known that the

MMTV-PyMT tumors lose ER expression in the advanced carcinoma stage. Since most of the *Malat1* ASO-treated tumors did not progress to advanced carcinomas, it is possible that they retained ERα expression. It remains to be further investigated whether the switch in the ER isoform confers stability to the protein.

Of particular note, *Sox5* was alternatively spliced, giving rise to an isoform that lacked the exon that encodes for a loop domain of this HMG transcription factor (Supplemental Fig. S6C,D). This finding was exciting, as motif analysis of differentially regulated genes upon *Malat1* knockdown also showed enrichment of *Sox5*-binding motifs in their promoters (Fig. 6F). Furthermore, many members of ECM signaling were also alternatively spliced, and *Itga2b* (Fig. 7D; Supplemental Fig. S6E) belonging to the integrin signaling pathway showed alternate 3′ splice site utilization that resulted in retention of part of an intron. This transcript was shown to be down-regulated in our gene expression analysis as well by qRT–PCR analysis.

Overall, *Malat1* knockdown affects both gene expression and alternative splicing of numerous protumorigenic signaling molecules and differentiation-related genes, resulting in a dramatic shift in mammary tumors to a highly differentiated less aggressive state.

Discussion

Malat1, a nuclear-localized lncRNA, is not required for normal development (Eissmann et al. 2012; Nakagawa et al. 2012; Zhang et al. 2012). Here, using a mouse model and 3D organotypic cultures, we demonstrate for the first time a functional role for *Malat1* in breast cancer progression. *Malat1* loss results in a dramatic differentiation of the primary tumor and a significant reduction in metastasis. These findings demonstrate a critical role for *Malat1* loss in redirecting the program of a poorly differentiated carcinoma to that of a highly differentiated "tissue." Importantly, systemic knockdown of *Malat1* using ASOs phenocopies genetic loss, thereby providing an exciting future avenue for exploring the use of *Malat1* ASOs in a therapeutic setting.

Malat1 *level increases upon cancer progression*

Consistent with our findings that *Malat1* plays a role in tumor progression, RNA-FISH analysis of paired human breast tumor samples and metastases indicated that while the level of *Malat1* is higher in the primary tumor than in the surrounding stroma, its level is further increased in the lung metastases (Fig. 7E). Of particular interest is the fact that some cells in the primary tumor exhibit a higher level of *Malat1*, and we suggest that it may be these cells that escape from the primary tumor and metastasize to the lungs. The up-regulation of *Malat1* may be triggered by physiological stress and/or oncogene activation. Interestingly, several previous studies in other cancers have found a correlation of *Malat1* levels with EMT transcription factors such as Zeb1 and Snail. Although we did not
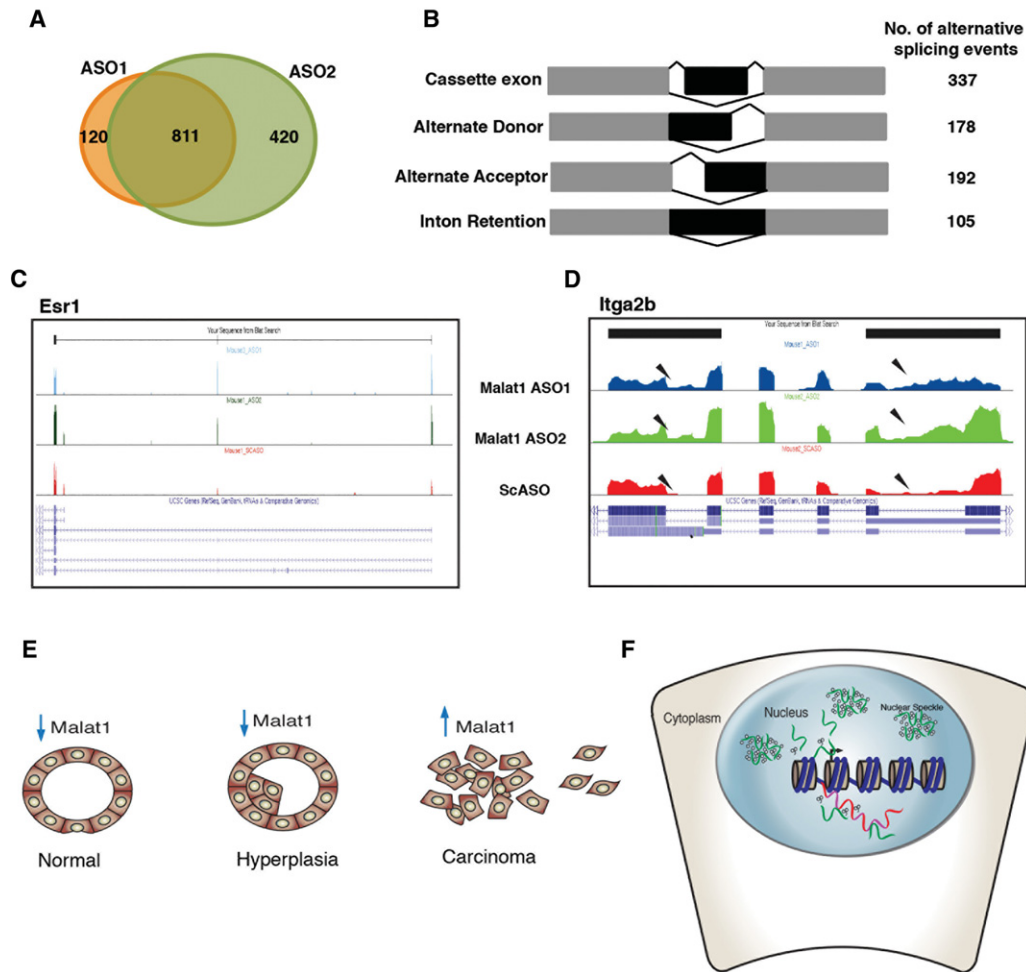
Figure 7. *Malat1* knockdown impacts alternative pre-mRNA splicing of the pre-mRNAs. (*A*) Venn diagram showing the total number of splicing changes in ASO1- and ASO2-treated tumors and tumor organoids with respect to scrambled-treated controls. Nearly 60% of changes overlap between ASO1- and ASO2-treated groups in at least two biological replicates. (*B*) Different types of splicing changes that are affected and the number of genes that are alternatively spliced upon *MALAT1* ASO treatment in each of them. (*C*) University of California at Santa Cruz (UCSC) screenshot showing an example of an alternatively spliced exon in the *Esr1* transcript. (*D*) UCSC screenshot showing an example of alternatively spliced exons in the *Itga2b* transcript resulting in partial intron retention. (*E*) Schematic of a working model of *Malat1* RNA levels. *Malat1* is expressed at a lower level in the differentiated mammary gland (normal) and early lesions (hyperplasia). *Malat1* up-regulation in mammary tumors (carcinoma) is concomitant with dedifferentiation and metastasis of the tumors. (*F*) Schematic of the proposed molecular mechanism. The lncRNA *Malat1* (green squiggles) shuttles between nuclear speckles and TSSs (arrowhead), where it can serve as a scaffold to regulate efficient transcription and alternative pre-mRNA splicing (red line).

observe changes in the expression of EMT transcription factors in our data sets, it is possible that *Malat1* expression could increase in cells that are undergoing EMT, and that may correlate well with those cells preferentially metastasizing. In this context, it has been shown previously that hypoxia-inducible factor *HIF1A* regulates *MALAT1* expression (Choudhry et al. 2014; Michalik et al. 2014). *Hif1a* is a major transcription factor that governs oxidative stress and regulates tumor progression and has also been shown to play a role in EMT (Semenza et al. 2003). In a number of cell culture studies, *Malat1* was found to be up-regulated upon stress such as serum starvation, hypoxia, and genotoxic stress, all of which are linked to tumor progression (Yang et al. 2011; Mizutani et al.

2012; Choudhry et al. 2014). Consistent with this, our findings demonstrated that *Malat1* loss in dedifferentiated primary tumors results in extensive alteration in gene expression, activating pathways that are involved in morphogenesis and differentiation.

Mammary gland differentiation has been shown to be regulated by GATA3 (Kouros-Mehr et al. 2008) and Stat signaling (Liu et al. 1997). Although we found that the Jak–Stat signaling pathway is altered in tumor organoids upon loss of *Malat1*, this change was not captured in the primary tumors, and *Gata3* was not differentially expressed in our data sets. Thus, additional factors likely regulate mammary tumor differentiation upon *Malat1* loss. Consistent with this possibility, ECM proteins and

integrin signaling are altered upon loss of *Malat1*, and differentiation markers of the mammary gland, such as casein genes, are up-regulated several-fold, resulting in secretion of these proteins within the cysts and thereby restoring a functional activity of the mammary gland. Interestingly, ECM proteins and integrin signaling have been previously shown to play a crucial role in the regulation of casein genes (Streuli et al. 1991, 1995; Pontier and Muller 2009), and prior studies have indicated that lactation confers cancer protection to the mammary gland due to differentiation of epithelial cells (Kotsopoulos et al. 2012).

Poorly differentiated primary tumors are often associated with a poor outcome and higher incidence of metastasis (for review, see Medema 2013). Therefore, the ability to differentiate primary tumors by loss or knockdown of *Malat1* significantly reduces the possibility that they will undergo EMT-like processes and become invasive. Multiple lines of evidence converge on this aspect of *Malat1* function, as its loss has been previously shown to reduce motility in cell lines and the homing behavior of lung cells in xenograft mouse models (Tano et al. 2010; Gutschner et al. 2013). Our findings add significantly to these prior observations by showing that loss of *Malat1* in tumor-bearing mice results in a 70% reduction in lung metastasis. We also found that *Malat1* loss inhibited branching morphogenesis in tumor organoids, consistent with its requirement for migration and local ECM remodeling of the organoids in Matrigel, a process that is similar to invasion and matrix degradation observed in vivo in malignant tumors (Ewald et al. 2008; Cheung et al. 2013). In addition, *Malat1* loss in both *MMTV-PyMT* and *Her2/neu*-amplified *MMTV-cre;Floxneo-neuNT* tumor organoids resulted in increased epithelial cell adhesion and loss of migration of cells, resulting in tightly packed spherical acinar structures. Given that the branching phenotype could be restored by addition of mouse full-length *Malat1*, *Malat1* is essential for this process, and the phenotype observed is specific for *Malat1*. Our data add significant support to the concept that organoids can provide a rapid means of assessing therapeutic potential in a patient-specific manner (Boj et al. 2015).

Malat1 *functions as a cotranscriptional splicing scaffold*

Although *Malat1* knockout mice exhibit no phenotype (Eissmann et al. 2012; Nakagawa et al. 2012; Zhang et al. 2012), upon *Malat1* knockout or knockdown in the *MMTV-PyMT* mammary cancer model, we observed changes in gene expression and pre-mRNA splicing of numerous cancer-relevant genes. Lack of significant overlap of differentially expressed genes upon *Malat1* loss among various studies supports a role for *Malat1* in a context-dependent manner. Based on cross-linking studies, it has been shown that *Malat1* is bound to either chromatin (West et al. 2014) or pre-mRNAs (Engreitz et al. 2014). Since it is well documented that transcription and pre-mRNA splicing are coupled processes (for review, see Bentley 2014), our data suggest that *Malat1* may act as a scaffold to coordinate these processes in a gene- and context-specific manner (Fig. 7F). The presence of *Malat1*

in nuclear speckles, domains that are commonly found near actively transcribing genes and are also enriched in splicing and transcription factors (for review, see Spector and Lamond 2011), could facilitate the function of *Malat1* at sites of transcription. Interestingly, based on comparisons between a CHART-seq data set from MCF7 cells that identified direct *MALAT1*-binding sites across the genome and our gene expression data set, we identified ~11% of our differentially expressed genes to be potential direct targets of *Malat1*, which is consistent with the possibility of *Malat1* coordinating expression of these genes. In line with this, we previously showed that loss of *Malat1* impairs the recruitment of SR splicing factors to a stably integrated transgene array (Bernard et al. 2010). It has also been previously shown that numerous splicing changes occur during tumor progression, giving rise to novel oncogenic splice variants (Venables et al. 2008; Eswaran et al. 2013). In this regard, SRSF1, a SR protein-splicing factor, can act as an oncoprotein that promotes breast cancer (Anczukow et al. 2012). During tumor progression, *Malat1* may facilitate efficient transcription and splicing of protumorigenic genes such as integrins, ECM proteins, and genes involved in migration and metastasis, leading to a more favorable outcome for the tumor. Thus, loss of *Malat1* results in altered transcription and pre-mRNA splicing events more consistent with the differentiated phenotype of the impacted tissue. Given the importance of estrogen signaling in luminal breast cancer and our observation that the estrogen receptor (*Esr1*) transcript was alternatively spliced in its 5′ UTR upon *Malat1* loss, it will be important in follow-up studies to determine whether *Esr1* isoform switching plays a role in the observed differentiation phenotype.

It is presently unclear whether *Malat1* binds to certain proteins or transcription factors to elicit its regulatory role. Previously published CLIP-seq (cross-linking immunoprecipitation [CLIP] combined with deep sequencing) and RNA pull-down studies from several groups have shown that *Malat1* binds to splicing factors such as SRSF1, TDP43, and PRC2 components, including EZH2 (Tripathi et al. 2010; Tollervey et al. 2011; Yang et al. 2011; Guil et al. 2012). Detailed motif analysis of the promoters of the differentially expressed genes in our data sets show them to be enriched for TCFCP2L1, SOX5, and E2A transcription factor-binding sites, which have established roles in tissue differentiation and pluripotency (Chen et al. 2008; Kamachi and Kondoh 2013; Ye et al. 2013). Therefore, we suggest that the specificity of the *Malat1*-responsive genes may be context-dependent and arise from the transcription factors that primarily regulate those genes. For example, *TCFCP2L1* has been shown to cooperate with the estrogen receptor family of transcription factors such as *ESRRB* (Boroviak et al. 2014) and has been shown to be associated with breast cancer metastasis to the lungs (Landemaine et al. 2008).

Malat1 *ASOs are a promising therapeutic*

Of potential clinical impact, we employed antisense-mediated knockdown using *Malat1*-specific ASOs in a

mouse model of metastatic mammary cancer. ASOs are currently in clinical trials for many diseases, including spinal muscular atrophy and Duchenne muscular dystrophy (Aartsma-Rus et al. 2004; Rigo et al. 2012). The in vivo efficacies of *Malat1* ASOs have been tested in primates, where >80% knockdown efficiency was achieved (Koller et al. 2011; Hung et al. 2013). Here we show that *Malat1* knockdown results in slower tumor proliferation and differentiation and significant reduction in metastasis, all recapitulating the phenotype of the *MMTV-PyMT; Malat1*^{−/−} genetic model, thus confirming the specificity of these ASOs. Future studies using patient-derived xenograft models as well as patient-derived tumor organoids will enable us to further study the efficacy of *Malat1* ASOs as a therapeutic to induce differentiation of primary human breast tumors and significantly reduce tumor progression.

Materials and methods

Animals

Animal experiments were carried out in the Cold Spring Harbor Laboratory Animal Shared Resource in accordance with Institutional Animal Care and Use Committee-approved procedures. *Malat1* knockout (C57BL/6) mice were generated as described previously (Zhang et al. 2012) and bred with *MMTV-PyMT* (C57BL/6) mice (Guy et al. 1992). *CAG::H2B-EGFP* mice (Hadjantonakis and Papaioannou 2004) were obtained from Jackson Laboratory and bred with *MMTV-PyMT* mice. *MMTV-Cre* and *Fl-neo-neu-NT* mice were obtained from Dr. William Muller (McGill University, Montreal) and were bred to generate *MMTV-Cre;Fl-neo-neu-NT*.

RNA in situ hybridization

RNA in situ hybridization was performed on formalin/PFA-fixed paraffin-embedded tissue sections using specific probes against human or mouse *Malat1* purchased from Affymetrix. The human tissue sections were obtained from Dr. Edi Brogi (Memorial Sloan Kettering Cancer Center). Both matched primary tumor sections/metastasis and unmatched array samples were scored for *MALAT1* level. The in situ hybridization protocol using View-RNA technology was performed according to the manufacturer's instructions (Affymetrix). Slides were scanned using an Aperio scanner, and the images were analyzed using Leica Scanscope software. Alternatively, nick-translated *Malat1* probes labeled with fluorescently conjugated dUTPs were used for RNA-FISH as described previously (Zhang et al. 2012). Images were captured using a DeltaVision microscope (GE). For all of the quantitative analysis, the fluorescent intensity profiles were obtained from at least five different random fields. When array spots were used for intensity measurement, the total intensity of the spot with ROI markup was used to estimate the signal intensity. The intensity values were binned to obtain the range, which was then used for plotting.

Organoid culture

Organoids from *MMTV-PyMT* and *MMTV-Cre;Flox neo-neu NT* tumors were prepared and cultured as described previously (Ewald 2013). Organoids were mixed with Matrigel and plated in 24-well Mat-Tek dishes. For ASO treatment, 500 nM *Malat1* ASO or scASO was added to 1 mL of organoid culture medium.

Images were acquired using a Zeiss Axio-Observer light microscope. For live-cell imaging, organoids from *MMTV-PyMT* or *MMTV-PyMT;CAG::H2B-EGFP* mice were treated with *Malat1* or ScASOs. At least five organoids per well were imaged in three dimensions over a period of 4 d at 15- or 30-min intervals using a Perkin-Elmer spinning-disc confocal microscope. Time-lapse images were processed using Volocity (PerkinElmer) and ImageJ (National Institutes of Health) software.

Electron microscopy

Organoids grown in Matrigel in 12-well culture dishes were fixed overnight with 2% glutaraldehyde and 2% paraformaldehyde in PBS. While in the multiwell dish, the samples were rinsed with distilled water and then post-fixed with 1% osmium tetroxide in 1.5% potassium ferrocyanide for 1 h. After a distilled water rinse, discs of Matrigel containing embedded organoids were lifted out of the culture dishes, cut into 2-mm × 10-mm × 4-mm pieces, and transferred into 20-mL glass scintillation vials. Samples were dehydrated in a graded series of ethanol and then rinsed in 100% acetone. Resin embedding was done with continuous agitation in 50% epon-araldite resin in acetone for 1 h and overnight incubation in 100% epon-araldite with agitation. Samples were then placed into BEEM capsules (placed flat into the cap end of a conical capsule made by cutting off the conical end), and the resin was polymerized overnight at 60°C in a vented oven. Samples were sectioned at 100 nm, collected on butvar-coated nickel slot grids (1-mm × 2-mm opening; Electron Microscopy Sciences), and counterstained with lead citrate. Sections were examined in a Hitachi H-7000 transmission electron microscope operated at 75 kV. Representative images were recorded on Kodak 4489 film. Images were scanned at 2400 dpi with an Epson Perfection VP750 Pro.

ASO treatment and tumor studies

The mice selected for ASO treatment were grouped based on age, initial tumor size, and separation of siblings into three cohorts. The ASOs against *Malat1* or ScASO were reconstituted at a concentration of 5 mg/mL in PBS and injected subcutaneously every day at a concentration of 25 mg/kg per day in a volume of ~125 μL for 5 d with a rest period of 2 d. Tumor growth was measured twice per week using calipers in a nonblinded fashion. Tumor volume was calculated based on the formula volume = width^2 × length/2. Mice were sacrificed after 8 wk of treatment, and tumors were removed and fixed in 4% PFA. Upon sacrifice, the lungs were also removed, and the macronodules were counted using a dissection microscope. Other internal organs, including the spleen, liver, kidney, and brain, were examined for metastasis or abnormalities using a dissection microscope.

Histology

Primary tumors and lungs were fixed in 4% PFA for up to 24 h and washed in PBS. Primary tumors were embedded in paraffin, sectioned, and stained with H&E. Slides were scanned using an Aperio slide scanner. The pathologist performed blind analyses to assess the histologic grade. The cystic area calculation was done using Aperio Scanscope software. After fixation, lungs were incubated in 20% sucrose overnight and embedded in OCT, and the lungs were cross-sectioned 2 mm apart. The lung sections were embedded horizontally to obtain serial sections of the entire lung, and H&E-stained sections were scanned with an Aperio image scope. The lung metastatic burden was calculated using Aperio Scanscope and ImageJ (National Institutes of Health) software.

Immunofluorescence

Immunofluorescence on the tumor cryosections was performed as described previously. Briefly, sections were washed in PBS and permeabilized for 5 min in 0.05% Triton X. The sections were blocked using 1% goat serum followed by incubation with primary antibody (Ki-67 from Vector Laboratories, E-cadherin from BD; β-casein was a gift from Dr. Mina Bissel) for 4 h to overnight at 4°C. Subsequently, the slides were washed with PBS + 0.01% Triton X. Finally, the sections were incubated in Alexa fluor-conjugated secondary antibodies (Jackson ImmunoResearch) followed by washes with PBS. The sections were stained with DAPI and mounted in 90% glycerol and 10% PBS plus PPD (paraphynelediamine). Images were acquired using a Zeiss LSM 710 or Zeiss Axio-Observer microscope. Ki-67 was quantified by counting the number of positive nuclei for every 100 nuclei from multiple fields on the slide to obtain the percentage of positive cells.

RNA-seq and analysis

Organoids generated from four MMTV-PyMT mice were cultured in 3D Matrigel domes in the presence of FGF2 for 6 d. The organoids were treated with 500 nM mock, ScASO, or *Malat1* ASOs. In addition, tumors were removed from MMTV-PyMT mice that had undergone injections with ScASO (three mice) or *Malat1* ASO1 (three mice) or ASO2 (four mice). Total RNA was extracted using TRIzol (Life Technologies) from both organoids and homogenized tumor tissue. Libraries for polyA$^+$ RNA-seq were prepared from 1 µg of RNA per sample using TruSeq chemistry (Illumina), multiplexed, and sequenced to obtain paired-end 101-base-pair (bp) reads on an Illumina HiSeq 2000 platform, resulting in 20 million to 86 million reads per library.

The quality of the raw data was evaluated using FastQC (http://www.bioinformatics.babraham.ac.uk/projects/fastqc), and reads were mapped to mm9 using STAR (Dobin et al. 2013), resulting in an overall mapping efficiency of >90%. The Gencode mV1 annotation set was used as a reference, and the reads per gene record were counted using the HTSeq package (Anders et al. 2015). Replicate analysis was carried out using edgeR (Robinson et al. 2010). Differential gene expression was performed with DESeq2 (Love et al. 2014). Functional analysis of KEGG pathways and gene ontology (GO) terms was carried out with the R/Bioconductor packages GAGE (Luo et al. 2009) and Pathview (Luo and Brouwer 2013). Motif analyses were performed using Homer (http://homer.salk.edu/homer; Heinz et al. 2010).

Splicing analysis

Alternative splicing, including cassette exons, alternative 3′/5′ splice site, and intron retention events, were identified and quantified using the SpliceTrap/SpliceDuo pipeline (Wu et al. 2011). This tool combines RNA-seq data with prebuilt transcript models to quantify the level of inclusion of every exon in a transcript. The transcript models are exon trios composed of alternative exon candidates with their annotated flanking exons. These were derived from the mm9 TXdb database, which accounts for a total of >230,000 exon trio models describing the alternative splicing of ∼190,000 mouse exons in ∼44,000 transcripts. SpliceTrap uses the Bowtie read aligner to align reads against TXdb. Biological replicates were analyzed independently, and alternative splicing events that were reproduced in at least two samples were selected (SpliceDuo FDR < 0.1). Inconsistent splicing events showing opposite splicing directions (skipping versus inclusion) were further removed.

RT-qPCR

One microgram of RNA was used to make cDNAs using oligo-dT primers. One-tenth the volume of the cDNA reaction mixture was used in the qPCR reaction containing 1× SYBR Green master mix (Applied Biosystems) and specific forward and reverse primers. The relative fold change was calculated using the $\Delta\Delta C_t$ method. The primers used were as follows: *Malat1* F (AACCAGTTTCCCCAGCTTTT) and *Malat1* R (CTACATTCCCACCCAGCACT).

Accession number

RNA-seq data presented in this study have been submitted to the NCBI Gene Expression Omnibus (GEO; http:// http://www.ncbi.nlm.nih.gov/geo) under accession number GSE67647

Acknowledgments

References

Aartsma-Rus A, Janson AA, Kaman WE, Bremmer-Bout M, van Ommen GJ, den Dunnen JT, van Deutekom JC. 2004. Antisense-induced multiexon skipping for Duchenne muscular dystrophy makes more sense. *Am J Hum Genet* **74:** 83–92.

Ades F, Zardavas D, Bozovic-Spasojevic I, Pugliano L, Fumagalli D, de Azambuja E, Viale G, Sotiriou C, Piccart M. 2014. Luminal B breast cancer: molecular characterization, clinical management, and future perspectives. *J Clin Oncol* **32:** 2794–2803.

Anczukow O, Rosenberg AZ, Akerman M, Das S, Zhan L, Karni R, Muthuswamy SK, Krainer AR. 2012. The splicing factor SRSF1 regulates apoptosis and proliferation to promote mammary epithelial cell transformation. *Nat Struct Mol Biol* **19:** 220–228.

Anders S, Pyl PT, Huber W. 2015. HTSeq—a Python framework to work with high-throughput sequencing data. *Bioinformatics* **31:** 166–169.

Andrechek ER, Hardy WR, Siegel PM, Rudnicki MA, Cardiff RD, Muller WJ. 2000. Amplification of the neu/erbB-2 oncogene in a mouse model of mammary tumorigenesis. *Proc Nat Acad Sci* **97:** 3444–3449.

Basham KJ, Kieffer C, Shelton DN, Leonard CJ, Bhonde VR, Vankayalapati H, Milash B, Bearss DJ, Looper RE, Welm BE. 2013. Chemical genetic screen reveals a role for desmosomal adhesion in mammary branching morphogenesis. *J Biol Chem* **288:** 2261–2270.

Bentley DL. 2014. Coupling mRNA processing with transcription in time and space. *Nat Rev Genet* **15:** 163–175.

Bergmann JH, Spector DL. 2014. Long non-coding RNAs: modulators of nuclear structure and function. *Curr Opin Cell Biol* **26:** 10–18.

Bernard D, Prasanth KV, Tripathi V, Colasse S, Nakamura T, Xuan Z, Zhang MQ, Sedel F, Jourdren L, Coulpier F, et al. 2010. A long nuclear-retained non-coding RNA regulates synaptogenesis by modulating gene expression. *EMBO J* **29:** 3082–3093.

Boj SF, Hwang CI, Baker LA, Chio II, Engle DD, Corbo V, Jager M, Ponz-Sarvise M, Tiriac H, Spector MS, et al. 2015. Organoid models of human and mouse ductal pancreatic cancer. *Cell* **160:** 324–338.

Boroviak T, Loos R, Bertone P, Smith A, Nichols J. 2014. The ability of inner-cell-mass cells to self-renew as embryonic stem cells is acquired following epiblast specification. *Nat Cell Biol* **16:** 516–528.

Bussemakers MJ, van Bokhoven A, Verhaegh GW, Smit FP, Karthaus HF, Schalken JA, Debruyne FM, Ru N, Isaacs WB. 1999. DD3: a new prostate-specific Gene, highly overexpressed in prostate cancer. *Cancer Res* **59:** 5975–5979.

Chen X, Xu H, Yuan P, Fang F, Huss M, Vega VB, Wong E, Orlov YL, Zhang W, Jiang J, et al. 2008. Integration of external signaling pathways with the core transcriptional network in embryonic stem cells. *Cell* **133:** 1106–1117.

Cheung KJ, Gabrielson E, Werb Z, Ewald AJ. 2013. Collective invasion in breast cancer requires a conserved basal epithelial program. *Cell* **155:** 1639–1651.

Choudhry H, Schodel J, Oikonomopoulos S, Camps C, Grampp S, Harris AL, Ratcliffe PJ, Ragoussis J, Mole DR. 2014. Extensive regulation of the non-coding transcriptome by hypoxia: role of HIF in releasing paused RNApol2. *EMBO Rep* **15:** 70–76.

Clemson CM, Hutchinson JN, Sara SA, Ensminger AW, Fox AH, Chess A, Lawrence JB. 2009. An architectural role for a nuclear noncoding RNA: NEAT1 RNA is essential for the structure of paraspeckles. *Mol Cell* **33:** 717–726.

Collette J, Hendrick JC, Jaspar JM, Franchimont P. 1986. Presence of α-lactalbumin, epidermal growth factor, epithelial membrane antigen, and gross cystic disease fluid protein (15,000 daltons) in breast cyst fluid. *Cancer Res* **46:** 3728–33.

Costa FF. 2007. Non-coding RNAs: lost in translation? *Gene* **386:** 1–10.

Derrien T, Johnson R, Bussotti G, Tanzer A, Djebali S, Tilgner H, Guernec G, Martin D, Merkel A, Knowles DG, et al. 2012. The Gencode v7 catalog of human long noncoding RNAs: analysis of their gene structure, evolution, and expression. *Genome Res* **22:** 1775–1789.

Djebali S, Davis CA, Merkel A, Dobin A, Lassmann T, Mortazavi A, Tanzer A, Lagarde J, Lin W, Schlesinger F, et al. 2012. Landscape of transcription in human cells. *Nature* **48:** 101–108.

Dobin A, Davis CA, Schlesinger F, Drenkow J, Zaleski C, Jha S, Batut P, Chaisson M, Gingeras TR. 2013. STAR: ultrafast universal RNA-seq aligner. *Bioinformatics* **29:** 15–21.

Eissmann M, Gutschner T, Hammerle M, Gunther S, Caudron-Herger M, Gross M, Schirmacher P, Rippe K, Braun T, Zornig M, et al. 2012. Loss of the abundant nuclear non-coding RNA MALAT1 is compatible with life and development. *RNA Biol* **9:** 1076–1087.

Ellis MJ, Ding L, Shen D, Luo J, Suman VJ, Wallis JW, Van Tine BA, Hoog J, Goiffon RJ, Goldstein TC, et al. 2012. Whole-genome analysis informs breast cancer response to aromatase inhibition. *Nature* **486:** 353–360.

The ENCODE Project Consortium. 2012. An integrated encyclopedia of DNA elements in the human genome. *Nature* **489:** 57–74.

Engreitz JM, Sirokman K, McDonel P, Shishkin AA, Surka C, Russell P, Grossman SR, Chow AY, Guttman M, Lander ES.

2014. RNA–RNA interactions enable specific targeting of noncoding RNAs to nascent Pre-mRNAs and chromatin sites. *Cell* **159:** 188–199.

Eswaran J, Horvath A, Godbole S, Reddy SD, Mudvari P, Ohshiro K, Cyanam D, Nair S, Fuqua SA, Polyak K, et al. 2013. RNA sequencing of cancer reveals novel splicing alterations. *Scientific Rep* **3:** 1689.

Ewald AJ. 2013. Isolation of mouse mammary organoids for long-term time-lapse imaging. *Cold Spring Harb Protoc* **2013:** 130–133.

Ewald AJ, Brenot A, Duong M, Chan BS, Werb Z. 2008. Collective epithelial migration and cell rearrangements drive mammary branching morphogenesis. *Dev Cell* **14:** 570–581.

Guffanti A, Iacono M, Pelucchi P, Kim N, Solda G, Croft LJ, Taft RJ, Rizzi E, Askarian-Amiri M, Bonnal RJ, et al. 2009. A transcriptional sketch of a primary human breast cancer by 454 deep sequencing. *BMC Genomics* **10:** 163.

Guil S, Soler M, Portela A, Carrere J, Fonalleras E, Gomez A, Villanueva A, Esteller M. 2012. Intronic RNAs mediate EZH2 regulation of epigenetic targets. *Nat Struct Mol Biol* **19:** 664–670.

Gupta RA, Shah N, Wang KC, Kim J, Horlings HM, Wong DJ, Tsai MC, Hung T, Argani P, Rinn JL, et al. 2010. Long non-coding RNA HOTAIR reprograms chromatin state to promote cancer metastasis. *Nature* **464:** 1071–1076.

Gutschner T, Hammerle M, Eissmann M, Hsu J, Kim Y, Hung G, Revenko A, Arun G, Stentrup M, Gross M, et al. 2013. The noncoding RNA MALAT1 is a critical regulator of the metastasis phenotype of lung cancer cells. *Cancer Res* **73:** 1180–1189.

Guy CT, Cardiff RD, Muller WJ. 1992. Induction of mammary tumors by expression of polyomavirus middle T oncogene: a transgenic mouse model for metastatic disease. *Mol Cell Biol* **12:** 954–961.

Hadjantonakis AK, Papaioannou VE. 2004. Dynamic in vivo imaging and cell tracking using a histone fluorescent protein fusion in mice. *BMC Biotechnol* **24:** 33.

Harrow J, Frankish A, Gonzalez JM, Tapanari E, Diekhans M, Kokocinski F, Aken BL, Barrell D, Zadissa A, Searle S, et al. 2012. Gencode: the reference human genome annotation for The ENCODE Project. *Genome Res* **22:** 1760–1774.

Heinz S, Benner C, Spann N, Bertolino E, Lin YC, Laslo P, Cheng JX, Murre C, Singh H, Glass CK. 2010. Simple combinations of lineage-determining transcription factors prime *cis*-regulatory elements required for macrophage and B cell identities. *Mol Cell* **38:** 576–589.

Herschkowitz JI, Simin K, Weigman VJ, Mikaelian I, Usary J, Hu Z, Rasmussen KE, Jones LP, Assefnia S, Chandrasekharan S, et al. 2007. Identification of conserved gene expression features between murine mammary carcinoma models and human breast tumors. *Genome Biol* **8:** R76.

Hung G, Xiao X, Peralta R, Bhattacharjee G, Murray S, Norris D, Guo S, Monia BP. 2013. Characterization of target mRNA reduction through in situ RNA hybridization in multiple organ systems following systemic antisense treatment in animals. *Nucleic Acid Ther* **23:** 369–378.

Hutchinson JN, Ensminger AW, Clemson CM, Lynch CR, Lawrence JB, Chess A. 2007. A screen for nuclear transcripts identifies two linked noncoding RNAs associated with SC35 splicing domains. *BMC Genomics* **8:** 39.

Ji P, Diederichs S, Wang W, Boing S, Metzger R, Schneider PM, Tidow N, Brandt B, Buerger H, Bulk E, et al. 2003. MALAT-1, a novel noncoding RNA, and thymosin β4 predict metastasis and survival in early-stage non-small cell lung cancer. *Oncogene* **22:** 8031–8041.

Kamachi Y, Kondoh H. 2013. Sox proteins: regulators of cell fate specification and differentiation. *Development* **140:** 4129–4144.

Koller E, Vincent TM, Chappell A, De S, Manoharan M, Bennett CF. 2011. Mechanisms of single-stranded phosphorothioate modified antisense oligonucleotide accumulation in hepatocytes. *Nucleic Acids Res* **39:** 4795–4807.

Kotsopoulos J, Lubinski J, Salmena L, Lynch HT, Kim-Sing C, Foulkes WD, Ghadirian P, Neuhausen SL, Demsky R, Tung N, et al. 2012. Breastfeeding and the risk of breast cancer in BRCA1 and BRCA2 mutation carriers. *Breast Cancer Res* **14:** R42.

Kouros-Mehr H, Bechis SK, Slorach EM, Littlepage LE, Egeblad M, Ewald AJ, Pai SY, Ho IC, Werb Z. 2008. GATA-3 links tumor differentiation and dissemination in a luminal breast cancer model. *Cancer Cell* **13:** 141–152.

Landemaine T, Jackson A, Bellahcene A, Rucci N, Sin S, Abad BM, Sierra A, Boudinet A, Guinebretiere JM, Ricevuto E, et al. 2008. A six-gene signature predicting breast cancer lung metastasis. *Cancer Res* **68:** 6092–6099.

Lin EY, Jones JG, Li P, Zhu L, Whitney KD, Muller WJ, Pollard JW. 2003. Progression to malignancy in the polyoma middle T oncoprotein mouse breast cancer model provides a reliable model for human diseases. *Am J Pathol* **163:** 2113–2126.

Lin R, Maeda S, Liu C, Karin M, Edgington TS. 2007. A large noncoding RNA is a marker for murine hepatocellular carcinomas and a spectrum of human carcinomas. *Oncogene* **26:** 851–858.

Liu X, Robinson GW, Wagner KU, Garrett L, Wynshaw-Boris A, Hennighausen L. 1997. Stat5a is mandatory for adult mammary gland development and lactogenesis. *Genes Dev* **11:** 179–186.

Love MI, Huber W, Anders S. 2014. Moderated estimation of fold change and dispersion for RNA-seq data with DESeq2. *Genome Biol* **15:** 550.

Luo W, Brouwer C. 2013. Pathview: an R/Bioconductor package for pathway-based data integration and visualization. *Bioinformatics* **29:** 1830–1831.

Luo W, Friedman MS, Shedden K, Hankenson KD, Woolf PJ. 2009. GAGE: generally applicable gene set enrichment for pathway analysis. *BMC Bioinformatics* **10:** 161.

Matsumoto K, Takayama N, Ohnishi J, Ohnishi E, Shirayoshi Y, Nakatsuji N, Ariga H. 2001. Tumour invasion and metastasis are promoted in mice deficient in tenascin-X. *Genes Cells* **6:** 1101–1111.

Medema JP. 2013. Cancer stem cells: the challenges ahead. *Nat Cell Biol* **15:** 338–344.

Michalik KM, You X, Manavski Y, Doddaballapur A, Zornig M, Braun T, John D, Ponomareva Y, Chen W, Uchida S, et al. 2014. Long noncoding RNA MALAT1 regulates endothelial cell function and vessel growth. *Circ Res* **114:** 1389–1397.

Mizutani R, Wakamatsu A, Tanaka N, Yoshida H, Tochigi N, Suzuki Y, Oonishi T, Tani H, Tano K, Ijiri K, et al. 2012. Identification and characterization of novel genotoxic stress-inducible nuclear long noncoding RNAs in mammalian cells. *PLoS One* **7:** e34949.

Nakagawa S, Ip JY, Shioi G, Tripathi V, Zong X, Hirose T, Prasanth KV. 2012. Malat1 is not an essential component of nuclear speckles in mice. *RNA* **18:** 1487–1499.

Pontier SM, Muller WJ. 2009. Integrins in mammary-stem-cell biology and breast-cancer progression—a role in cancer stem cells? *J. Cell Sci* **122:** 207–214.

Prasanth KV, Spector DL. 2007. Eukaryotic regulatory RNAs: an answer to the 'genome complexity' conundrum. *Genes Dev* **21:** 11–42.

Prensner JR, Chinnaiyan AM. 2011. The emergence of lncRNAs in cancer biology. *Cancer Discov* **1:** 91–407.

Prensner JR, Iyer MK, Balbin OA, Dhanasekaran SM, Cao Q, Brenner JC, Laxman B, Asangani IA, Grasso CS, Kominsky HD, et al. 2011. Transcriptome sequencing across a prostate cancer cohort identifies PCAT-1, an unannotated lincRNA implicated in disease progression. *Nat Biotechnol* **29:** 742–749.

Prensner JR, Iyer MK, Sahu A, Asangani IA, Cao Q, Patel L, Vergara IA, Davicioni E, Erho N, Ghadessi M, et al. 2013. The long noncoding RNA SChLAP1 promotes aggressive prostate cancer and antagonizes the SWI/SNF complex. *Nat Genet* **45:** 1392–1398.

Rigo F, Hua Y, Krainer AR, Bennett CF. 2012. Antisense-based therapy for the treatment of spinal muscular atrophy. *J Cell Biol* **199:** 21–25.

Rinn JL, Chang HY. 2012. Genome regulation by long noncoding RNAs. *Ann Rev Biochem* **81:** 145–166.

Robinson MD, McCarthy DJ, Smyth GK. 2010. edgeR: a Bioconductor package for differential expression analysis of digital gene expression data. *Bioinformatics* **26:** 139–140.

Sachs N, Clevers H. 2014. Organoid cultures for the analysis of cancer phenotypes. *Curr Opin Genet Dev* **24:** 68–73.

Sato T, Clevers H. 2013. Growing self-organizing mini-guts from a single intestinal stem cell: mechanism and applications. *Science* **340:** 1190–1194.

Schnitt SJ. 2010. Classification and prognosis of invasive breast cancer: from morphology to molecular taxonomy. *Modern Pathol* **23:** S60–S64.

Semenza GL. 2003. Targeting HIF-1 for cancer therapy. *Nat Rev Cancer* **3:** 721–732.

Spector DL, Lamond AI. 2011. Nuclear speckles. *Cold Spring Harbor Persp Biol* **3:** a000646.

Streuli CH, Bailey N, Bissell MJ. 1991. Control of mammary epithelial differentiation: basement membrane induces tissue-specific gene expression in the absence of cell–cell interaction and morphological polarity. *J Cell Biol* **115:** 1383–1395.

Streuli CH, Edwards GM, Delcommenne M, Whitelaw CB, Burdon TG, Schindler C, Watson CJ. 1995. Stat5 as a target for regulation by extracellular matrix. *J Biol Chem* **270:** 21639–21644.

Subramanian A, Tamayo P, Mootha VK, Mukherjee S, Ebert BL, Gillette MA, Paulovich A, Pomeroy SL, Golub TR, Lander ES, et al. 2005. Gene set enrichment analysis: a knowledge-based approach for interpreting genome-wide expression profiles. *Proc Natl Acad Sci* **102:** 15545–15550.

Tano K, Mizuno R, Okada T, Rakwal R, Shibato J, Masuo Y, Ijiri K, Akimitsu N. 2010. MALAT-1 enhances cell motility of lung adenocarcinoma cells by influencing the expression of motility-related genes. *FEBS Lett* **584:** 4575–4580.

Teplova M, Minasov G, Tereshko V, Inamati GB, Cook PD, Manoharan M, Egli M. 1999. Crystal structure and improved antisense properties of 2′-O-(2-methoxyethyl)-RNA. *Nat Struct Biol* **6:** 535–539.

Tollervey JR, Curk T, Rogelj B, Briese M, Cereda M, Kayikci M, Konig J, Hortobagyi T, Nishimura AL, Zupunski V, et al. 2011. Characterizing the RNA targets and position-dependent splicing regulation by TDP-43. *Nat Neuro* **14:** 452–458.

Tripathi V, Ellis JD, Shen Z, Song DY, Pan Q, Watt AT, Freier SM, Bennett CF, Sharma A, Bubulya PA, et al. 2010. The nuclear-retained noncoding RNA MALAT1 regulates alternative splicing by modulating SR splicing factor phosphorylation. *Mol Cell* **39:** 925–938.

Tseng YY, Moriarity BS, Gong W, Akiyama R, Tiwari A, Kawakami H, Ronning P, Reuland B, Guenther K, Beadnell TC,

et al. 2014. PVT1 dependence in cancer with MYC copy-number increase. *Nature* **512:** 82–86.

Venables JP, Klinck R, Bramard A, Inkel L, Dufresne-Martin G, Koh C, Gervais-Bird J, Lapointe E, Froehlich U, Durand M, et al. 2008. Identification of alternative splicing markers for breast cancer. *Cancer Res* **68:** 9525–9531.

Watson CJ, Campbell JJ. 2009. Three-dimensional culture models of mammary gland. *Organogenesis* **5:** 43–49.

West JA, Davis CP, Sunwoo H, Simon MD, Sadreyev RI, Wang PI, Tolstorukov MY, Kingston RE. 2014. The long noncoding RNAs NEAT1 and MALAT1 bind active chromatin sites. *Mol Cell* **55:** 791–802.

Wilusz JE, Freier SM, Spector DL. 2008. 3′ end processing of a long nuclear-retained noncoding RNA yields a tRNA-like cytoplasmic RNA. *Cell* **135:** 919–932.

Wilusz JE, Sunwoo H, Spector DL. 2009. Long noncoding RNAs: functional surprises from the RNA world. *Gene Dev* **23:** 1494–1504.

Wu J, Akerman M, Sun S, McCombie WR, Krainer AR, Zhang MQ. 2011. SpliceTrap: a method to quantify alternative splicing under single cellular conditions. *Bioinformatics* **27:** 3010–3016.

Yamada K, Kano J, Tsunoda H, Yoshikawa H, Okubo C, Ishiyama T, Noguchi M. 2006. Phenotypic characterization of endometrial stromal sarcoma of the uterus. *Cancer Sci* **97:** 106–12.

Yang L, Lin C, Liu W, Zhang J, Ohgi KA, Grinstein JD, Dorrestein PC, Rosenfeld MG. 2011. ncRNA- and Pc2 methylation-dependent gene relocation between nuclear structures mediates gene activation programs. *Cell* **147:** 773–788.

Ye S, Li P, Tong C, Ying QL. 2013. Embryonic stem cell self-renewal pathways converge on the transcription factor Tfcp2l1. *EMBO J* **32:** 2548–2560.

Zhan L, Rosenberg A, Bergami KC, Yu M, Xuan Z, Jaffe AB, Allred C, Muthuswamy SK. 2008. Deregulation of scribble promotes mammary tumorigenesis and reveals a role for cell polarity in carcinoma. *Cell* **135:** 865–878.

Zhang B, Arun G, Mao YS, Lazar Z, Hung G, Bhattacharjee G, Xiao X, Booth CJ, Wu J, Zhang C, et al. 2012. The lncRNA Malat1 is dispensable for mouse development but its transcription plays a *cis*-regulatory role in the adult. *Cell Rep* **2:** 111–123.